Pitching single focus confocal data analysis one photon at a time with Bayesian nonparametrics

Meysam Tavakoli
Department of Physics, Indiana University-Purdue University Indianapolis, IN 46202.

Sina Jazani, Ioannis Sgouralis
Center for Biological Physics, Department of Physics, Arizona State University, Tempe, AZ 85287

Omer M. Shafraz, Sanjeevi Sivasankar
Department of Biomedical Engineering, University of California, Davis, CA 95616

Bryan Donaphon
Biodesign Institute, Arizona State University, Tempe, AZ 85287

Marcia Levitus
Center for Biological Physics, Department of Physics,
Arizona State University, Tempe, AZ 85287
Biodesign Institute, Arizona State University, Tempe, AZ 85287
School of Molecular Sciences,
Arizona State University, Tempe, AZ 85287

Steve Pressé*
Center for Biological Physics, Department of Physics,
Arizona State University, Tempe, AZ 85287
School of Molecular Sciences,
Arizona State University, Tempe, AZ 85287
Department of Physics,
Arizona State University, Tempe, AZ 85287

(Dated: August 24, 2019)

Fluorescence time traces are used to report on dynamical properties of biomolecules. The basic unit of information drawn from these traces is the individual photon. Single photons carry instantaneous information from the biomolecule, from which they are emitted, to the detector on timescales as fast as microseconds. Thus from confocal microscope it is theoretically possible to monitor biomolecular dynamics at such timescales. In practice, however, signals are stochastic and in order to deduce dynamical information through traditional means–such as fluorescence correlation spectroscopy (FCS) and related techniques–fluorescence signals are collected and temporally auto-correlated over several minutes. So far, it has been impossible to analyze dynamical properties of biomolecules on timescales approaching data acquisition as this demands that we estimate the instantaneous number of biomolecules emitting photons and their positions within the confocal volume. The mathematical structure of this problem demands that we abandon the normal ("parametric") Bayesian paradigm. Here, we exploit novel mathematical tools, namely Bayesian nonparametrics, that allow us to deduce in a principled fashion the same information normally deduced from FCS but from the direct analysis of significantly smaller datasets starting from individual photon arrivals. We discuss the implications of this method in helping dramatically reduce phototoxic damage on the sample and the ability to monitor out-of-equilibrium processes.

I. INTRODUCTION

Methods to capture static biomolecular structures, such as super-resolution microscopy [33, 48, 62], provide only snapshots of life in time. Yet life is dynamical and obtaining a picture of life in action–one that captures diffraction-limited biomolecules as they move, assemble into and disassemble from larger bimolecular complexes–remains an important challenge [55]. In fact, the creative insights directly leading to fluorescence correlation spectroscopy (FCS) [27, 64]–and related methods such as FCS-FRET [78, 95] and FCCS [84]–have shown that deciphering dynamical information from biomolecules does not demand spatial resolution or spatial localization.

The key idea behind these methods is to illuminate a small region of space inhomogeneously. As fluorescently-

* Second.Author@institution.edu

labeled biomolecules diffuse across this illuminated volume, they emit photons (i.e., they fluoresce) in a way that is proportional to the laser intensity at their respective locations [52]. Single photon detectors, often photomultiplier tubes or avalanche photodiodes, are then used to record these photons. In principle, with the appropriate electronics, photons can be recorded within μs-ms (depending on the detector, laser intensity, label emission rates and the concentration of labeled biomolecules) and this suggests that information on biomolecular diffusion could be drawn from the data on timescales approaching data acquisition.

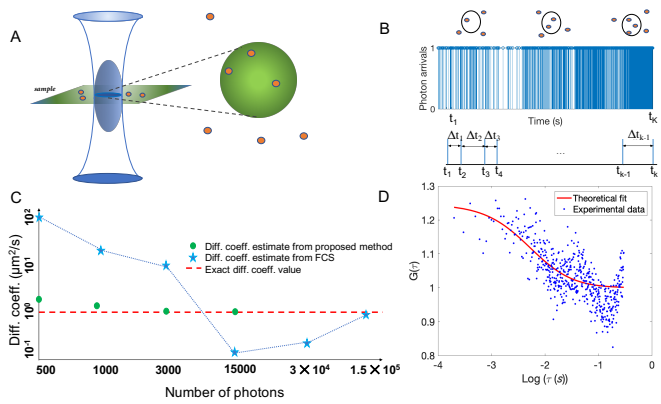

FIG. 1. **Confocal methods have the potential to reveal dynamical information on biomolecules on fast, photon-detection, timescales**. (A) Schematic of an illuminated confocal volume (blue) aligned along the z-axis with labeled biomolecules emitting photons based on their location within that volume. A slice perpendicular to the z-axis is shown in green with the instantaneous position of biomolecules shown in red. (B) Sample synthetic photon arrival trajectory with diffusion coefficient of 1 $\mu m^2/s$ and its representation in terms of inter-arrival times. The synthetic trace is produced using 4 single biomolecules for a total time of 30 ms (with a total of about 1500 photon arrivals) and background and particle photon emission rates 10^3 photons/s and 4×10^4 photons/s respectively. (C) Comparison between diffusion coefficient estimates using our current method, explained later, and FCS as a function of the number of photons used in the analysis. (D) Auto-correlation curve, $G(\tau)$, of sample synthetic trace in (B). Normally, in FCS analysis, much longer traces would be used to generate much smoother $G(\tau)$'s that would then be fitted to determine diffusion coefficients.

The fundamental quantity measured in a single focus confocal setups are individual photon arrival times, from which photon inter-arrival times, i.e., the intervals between adjacent photon arrivals, can be readily obtained. If we were imaging biomolecules fixed in space and under homogeneous (uniform) illumination, these inter-arrival times–excluding other experimental and label artifacts such as detector noise, background photons, and label photo-physical kinetics–would be identically distributed and so uncorrelated with each other. However, inter-arrival times derived from conventional single focus confocal experiments encode the number of biomolecules in the vicinity of the confocal volume, their diffusional dynamics, their position with respect to the confocal volume center in addition to experimental artifacts. Consequently, inter-arrival times are correlated with each other, and in principle these correlations can be exploited to infer dynamical quantities of the underlying biomolecular system.

In practice, these correlations are exploited by collecting billions of photons over several minutes [79] and temporally auto-correlating the fluorescence intensity measurements [14, 27, 32, 64]. For sufficiently long time traces, the stochasticity in the number of labeled biomolecules contributing photons as well as their positions in the illuminated volume (and thus their photon emission rates) are averaged out. As such, the expression for the fluorescence intensity time-autocorrelation takes a simple form that–under strong assumptions on the illuminated confocal volume's geometry and the biomolecule's point spread function (PSF)–can be summarized in simple analytic formulas. As we will see, our method can treat any known confocal volume geometry.

In these formulas [14, 27, 32, 64], for long enough time traces–and provided dynamical processes under observation are stationary over the long data acquisition times–only the average number of illuminated biomolecules over the entire trace matters. This average number appears as a pre-factor in the fluorescence intensity time autocorrelation. This observation suggests that, if we were to analyze single photon arrivals, then we would need to determine the stochastic number of biomolecules contributing photons.

A critical disadvantage of auto-correlative methods across all of FCS and related methods remains the stark timescale separation between data collection and the timescale required to deduce dynamical information; see Fig. (1). A method that could take direct advantage of single photon arrivals could reveal dynamical information on timescales several orders of magnitude faster than traditional FCS analysis. As a result, rapid or non-equilibrium processes could be studied or phototoxicity damage could be reduced dramatically [62, 65, 77, 94] simply by reducing the time during which the sample is kept under illumination. This would be especially relevant for *in vivo* FCS applications [25, 74, 85, 96]. Alternatively, data collected on timescales far exceeding those typically required by auto-correlative analysis methods in FCS could be used to deduce subtle dynamical changes or slight differences in diffusion coefficients if multiple species diffuse simultaneously through the confocal volume.

Previously proposed methods to analyze single photon measurements [2, 38, 39, 43, 70, 76, 99] make assumptions that render them inappropriate for imaging biomolecules (or particles, more broadly speaking) moving through inhomogeneously illuminated volumes [38]. For example, they may assume that the biomolecules are fixed in space. Thus the photon inter-arrival times reflect the

biomolecular conformational transitions in fluorescence resonance energy transfer (FRET) [38–40] but not the non-stationarity in the inter-photon arrival statistics inherently introduced by biomolecular diffusion across an inhomogeneously illuminated volume [23, 24, 37, 39].

By contrast, to be able to estimate the diffusion coefficient of labeled biomolecules used in a confocal experiment, we must be able to determine the number of biomolecules responsible for the observed photon arrival time trace. So far, the tools to deduce this information from photon time traces have been unavailable. Otherwise, naively, many biomolecules with small diffusion coefficients emitting photons at the periphery of the illuminated confocal volume could be mistaken for fewer biomolecules with higher diffusion coefficients in the most illuminated region (the center) of the confocal volume. Misidentifying the number of biomolecules, say, or incorrectly assessing their positions may give rise to incorrect estimates of quantities such as diffusion coefficients; see Fig. (2).

More concretely, formulating a likelihood to estimate the diffusion coefficient [7] from photon arrival data demands that we know the number of biomolecules contributing photons as well as their locations across time. As the number of biomolecules instantaneously located within the confocal volume are unknown, all reasonable possibilities would need to be considered and rank-ordered using expensive pre- or post-processing model selection heuristics [55, 92]. This has not been achieved yet, in part, because it is computationally infeasible to consider all possible biomolecule numbers across all possible positions with any possible diffusion coefficient.

Analyzing single photons arrivals from a confocal setup to derive dynamical information therefore demands fundamentally new tools. The single photon analysis methods mentioned earlier use parametric representations (i.e., fixed and known biomolecule numbers). Yet, those are precisely the assumptions we need to lift in analyzing single photon level data from confocal experiments.

The conceptually new mathematical framework that we propose can winnow down infinite possibilities (i.e., infinite populations of biomolecules potentially contributing photons) to a finite, manageable, number in a mathematically exact manner. Such a framework avoids compromising temporal resolution and allows us to directly deduce dynamical information from single photons. This framework is Bayesian nonparametrics (BNPs) [31], a powerful set of tools still in its infancy and largely unknown to the Physical Sciences. Within BNPs, we use mathematical devices, such as the beta-Bernoulli process, that have only been proposed in the last few years [1, 15, 71].

BNPs are poised to reshape our interpretation of inherently noisy biophysical data as they directly deal with model uncertainty (in this case, it is the uncertainty in the number of biomolecules). Contrary to traditional (parametric) Bayesian methods [34, 46, 55, 98], BNPs begin by assuming models infinite in size. That is, they

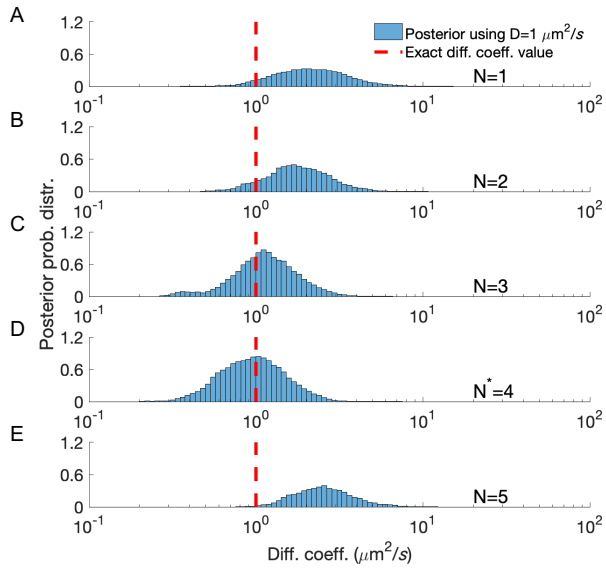

FIG. 2. **Estimates of diffusion coefficients from photon arrival traces strongly depend on the number of biomolecules we believe are contributing to the trace. Thus we need systematic tools to estimate biomolecular numbers on-the-fly if we are to deduce diffusion coefficients from mere thousands of photons**. Here, in generating synthetic data we use a 3D Gaussian volume of size $\omega_{xy} = 0.3\mu m$ nm and $\omega_z = 1.5\mu m$. The synthetic trace is produced using a total of 4 biomolecules for a total time of 30 ms (with a total of about 1800 photon arrivals) and generated by using a diffusion coefficient of $1\mu m^2/s$ and background and particle photon emission rates of 10^3 photons/s and 4×10^4 photons/s respectively. To estimate the D parametrically, we start with the following number of biomolecules, N =1 (A), N=2 (B), N=3 (C), N=4 (D), and N=5 (E). The good fit provided by (D)–and the mismatch in the peak of the posterior distribution over the diffusion coefficient and correct value of the diffusion coefficient (dotted line) in all others–underscores why it will be critical for us, or any method analyzing single photon data in the context of confocal experiments, to correctly estimate the number of biomolecules contributing to the trace in order to deduce dynamical parameters such as diffusion coefficients. In the supplementary information, we redo the analysis shown here with a higher diffusion coefficient.

begin by assuming an infinite number of biomolecules contributing photons. Then, among other quantities, they deduce full posteriors over model sizes from the data available. Concretely, for the case of our single photon time traces otherwise analyzed using FCS (see description in caption of Fig. (1)), they assign posterior probabilities over a number of quantities including all possible number of biomolecules responsible for the data and their associated locations at each photon arrival. Thus, BNPs turn the otherwise difficult problem of model-selection–that is, determining how many biomolecules, say, contribute photons–into a parameter estimation problem.

While BNPs have had a deep impact on Data Sci-

ence since their inception, they are relatively new to Biophysics with a handful of papers [18, 47, 73] published to date using BNPs in Biophysical applications [50, 55, 87–90, 92].

II. MATERIALS AND METHODS

Here we describe the mathematical formulation of our method. We begin with the overall input which consists of photon inter-arrival times, $\boldsymbol{\Delta t} = (\Delta t_1, \Delta t_2, \ldots, \Delta t_{K-1})$ where Δt_k denotes the time interval between adjacent observations of photons which occur at times t_k and t_{k-1}, for $k = 1, \ldots, K-1$. We also use as an input the confocal volume shape and background photon emission rate. The confocal volume shape is usually calibrated (normally under the restriction of a Gaussian PSF) experimentally by analyzing species of known diffusion coefficient (determined from other methods), while the background photon emission rate is determined by analyzing a time trace drawn from a control confocal experiment void of fluorophores within the sample.

To derive estimates for the diffusion coefficient, we need to determine intermediate quantities which include: i) particle photon emission rates of biomolecular labels; and, most importantly, ii) the unknown number biomolecules contributing photons to the trace as well as their location with respect to the center of the illuminated confocal volume. Below, we explain each one of these steps in some detail. More details and an implementation of the whole method are available in the Supplementary Information (SI). In addition, source code and a GUI version of our implementation are provided online through the SI.

A. Model Description

We begin with the distribution according to which the kth photon observation, Δt_k, is derived

$$\Delta t_k \sim \text{Exponential}\left(\mu_k\right). \tag{1}$$

Accordingly, Δt_k follows an exponential probability distribution [40, 75] with rate μ_k. In fact, the rate μ_k gathers the photon emission rates of all biomolecules which depend on their respective locations relative to the confocal volume center (see below) [12]. In addition to the biomolecule photon emissions rates, μ_k also includes background photons

$$\mu_k = \mu_{back} + \sum_n \mu_k^n \tag{2}$$

where $\sum_n \mu_k^n$ is the photon emission rates μ_k^n gathered from individual biomolecules, that we index with $n = 1, 2, \ldots,$ and μ_{back} is a background photon emission rate assumed uniform over time. In fact, μ_k^n and μ_{back} are the emission rates of detected photons, which due to

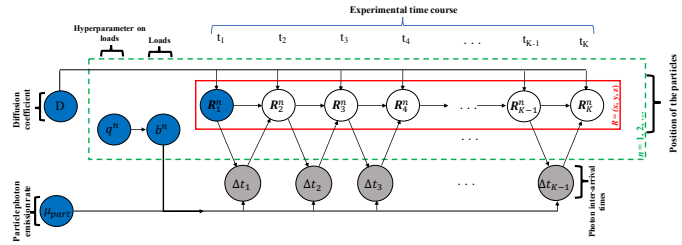

FIG. 3. **Graphical model of the formulation used in the analysis of photon arrivals trace**. Biomolecules, labeled by $n = 1, 2, \ldots,$ evolve over the experimental time course, with discrete time indexed by $k = 1, 2, \ldots, K-1$. Here, $R_k^n = (x_k^n, y_k^n, z_k^n)$ indicates the location of biomolecule n in Cartesian space at time t_k; μ_{part} marks the particle photon emission rate obtained by individual biomolecular labels. During the experiment, only a single observation (inter-arrival time) Δt_k is recorded, thereby combining photon emissions between t_k and t_{k-1} from every biomolecular label and background at each step. The diffusion coefficient D specifies the evolution of the biomolecular locations which influence the photon emission rates and eventually the recorded photon inter-arrival times Δt_k. The load, or auxiliary variables b^n, and corresponding prior weights q^n, are introduced in order to infer the unknown biomolecule population size. In the graphical model, the known or measured data is highlighted by dark shaded circles and model variables, which require prior probability, are showed by blue circles. For details about the graphical model see SI.

optical and detector limitations, are typically lower than the total photon emission rates [66, 67].

Next, we incorporate the dependency of the emission rate on location [4, 20, 102] with other effects such as camera pinhole shape and size, the laser intensity, laser wavelength, and quantum yield [12] into a characteristic PSF that combines excitation and emission PSFs and, just as with traditional FCS applications [14, 27, 32, 64], we use a 3D Gaussian geometry [52]

$$\mu_k^n = \mu_{part} \exp\left(-2\frac{(x_k^n)^2 + (y_k^n)^2}{\omega_{xy}^2} - 2\frac{(z_k^n)^2}{\omega_z^2}\right) \tag{3}$$

where the parameter μ_{part} indicates the particle emission rate of detected photons for a single biomolecule, which happens when the biomolecule is at the center of the confocal volume where illumination is highest. We mention here that, in the Results section, we report by common convention the emission rates which differ from the particle emission rates (i.e., those achieved at the center of the confocal volume) by a factor of $\sqrt{8}$. The difference is explained in the SI.

In (3), ω_{xy} and ω_z are semi-minor and semi-major axes of the confocal volume.

Finally, the dynamics of the system are assumed purely

diffusive

$$x_k^n \sim \text{Normal}(x_{k-1}^n, 2D\Delta t_{k-1}) \quad (4)$$
$$y_k^n \sim \text{Normal}(y_{k-1}^n, 2D\Delta t_{k-1}) \quad (5)$$
$$z_k^n \sim \text{Normal}(z_{k-1}^n, 2D\Delta t_{k-1}) \quad (6)$$

where D is the diffusion coefficient, which we assume identical for all biomolecules. As we explain in the SI, these probabilities result directly from the solution to the diffusion equation with open boundaries.

A graphical summary of the entire formulation is shown on Fig. (3).

B. Model Inference

All quantities which we infer–such as the diffusion coefficient, D, biomolecular locations through time, (x_k^n, y_n^k, z_n^k) and the particle photon emission rate μ_{part}– are introduced as model variables in the preceding formulation. We estimate these variables within the Bayesian paradigm [34, 55, 92]. The model parameters such as D and μ_{part} require priors. Additionally, we have to consider priors on the initial biomolecular locations, i.e., at the time of the very first photon arrival, (x_1^n, y_1^n, z_1^n). Options for these priors are straightforward and, for computational convenience, we adopt the distributions described in the SI.

Before we proceed any further, we revise (7) as

$$\mu_k^n = b^n \mu_{part} \exp\left(-2\frac{(x_k^n)^2 + (y_k^n)^2}{\omega_{xy}^2} - 2\frac{(z_k^n)^2}{\omega_z^2}\right). \quad (7)$$

The variables b^n, defined for each model biomolecule, take only values 1 or 0 where we have $b^n = 0$ when the nth biomolecule does not contribute photons to the measurements. This indicator variable allows us to define an arbitrarily large population of model biomolecules, technically an infinite number. The ability to recruit, from a potentially infinite pool of biomolecules, the precise number that contributes to the measured trace is the chief reason we need to abandon the parametric Bayesian paradigm.

After introducing b^n, we can estimate the number of biomolecules that contribute photons, i.e., those biomolecules where $b^n = 1$, simultaneously with the rest of the parameters simply by treating each b^n as a separate parameter and estimating its value.

To estimate b^n, we consider a Bernoulli prior with a Beta hyper-prior in order to learn how many biomolecules are active

$$b^n | q^n \sim \text{Bernoulli}(q^n) \quad (8)$$
$$q^n \sim \text{Beta}(A_q, B_q) \quad (9)$$

where A_q and B_q are (hyper-hyper-)parameters specifically chosen to allow $n \to \infty$. Both steps can be combined and are termed the Beta-Bernoulli process [1, 15, 71]; see SI for more details.

With these priors, we can now form a joint posterior probability $p(D, \mu_{part}, (x_k^n, y_k^n, z_k^n, b^n, q^n)_k^n | \mathbf{\Delta} t)$ including all unknown variables which we want to determine. The nonlinearities in the PSF, in terms of variables $(x_k^n, y_k^n, z_k^n)_k^n$, and the nonparametric prior on $(b^n, q^n)^n$ exclude analytic forms for our posterior. For this reason, we adopt Markov Chain Monte Carlo (MCMC) computational schemes [34, 53, 80] that can be used to generate pseudo-random samples from this posterior. The scheme is described in the SI and a working implementation is given in the single biomolecule.

C. Acquisition of Synthetic Data for Figs. (4)-(7)

We obtain the synthetic data presented in the Results by standard pseudo-random computer simulations [6, 30, 42, 45, 49] that simulate Brownian motion of point biomolecules through a typical illuminated confocal volume. We provide finer details and complete parameter choices in the SI.

D. Acquisition of Experiment data for Figs. (8)-(10)

Biomolecule solutions were made by suspending Cy3 dye in glycerol/buffer (pH 7.5, 10 mM Tris-HCl, 100 mM NaCl and 10 mM KCl, 2.5 mM $CaCl_2$) at various v/v, to a final concentration of either 100 pM or 1 nM. The biomolecule solution was placed in a glass-bottomed fluid-cell, assembled on a custom designed confocal microscope [58] and a 532 nm laser beam was focused to a diffraction-limited spot on the glass coverslip of the fluid-cell using a 60x, 1.42 N.A., oil-immersion objective (Olympus). Emitted fluorescence was gathered by the same objective and focused onto the detection face of a Single Photon Avalanche Diode (SPAD, Micro Photon Devices) that has a highest count rate of 11.8 Mc/s. A bandpass filter was set in front of the detector relayed only the fluorescence from Cy3 and blocked the back-scattered excitation light. TTL pulses, triggered by the individual photon arrivals on the SPAD, were timestamped and registered at 80 MHz using a field programmable gate array (FPGA, NI Instruments) using custom LabVIEW software [82].

E. Acquisition of Experimental data for Fig. (11)

The excitation source was a supercontinuum fiber laser Fianium WhiteLase SC480 (NKT Photonics, Birkerod, Denmark) operating at a repetition rate of 40 MHz. The excitation wavelength (550 nm) was selected by an acousto-optic tunable filter (AOTF), and the exiting beam was collimated and expanded by approximately a factor of three to slightly overfill the back aperture of the objective lens. The light was reflected into the objective

lens (Zeiss EC Plan-Neofluar 100x oil, 1.3 NA pol M27, Thornwood, NY, USA) by a dichroic mirror (Chroma 89016bs). The same objective was used to collect the fluorescence from the sample, and passed through a band pass filter (Chroma ET575/50m) before being focused into a position motorized pinhole wheel set at 25 μm. The output of the pinhole was focused on a multimode hybrid fiber optic patch cable (M18L01, Thorlabs, NJ, USA) which was coupled to a single-photon avalanche diode (SPCM AQRH-14, Excelitas Technologies, Quebec, Canada). The detected photons were recorded by a TimeHarp 200 time-correlated single photon counting board (PicoQuant, Berlin, Germany) operating in T3 mode. The sample ($\approx$50 μL) was contained in a perfusion chamber gasket (CoverWell) adhered on a glass coverslip.

The sample was 20 nM 5-Carboxytetramethylrhodamine (5-TAMRA, purchased from Sigma-Aldrich, USA) dissolved in doubly distilled water at room temperature. Acquisition time was 10 minutes; 4.61×10^6 photons were recorded in the experiment. Data was analyzed using the Sympho Time 64 software from PicoQuant (Berlin, Germany). The autocorrelation function was calculated from the photon arrival data and background and after pulsing correction were performed as implemented in the software using the microscopic delay times (measured relative to the onset of the excitation pulse).

III. RESULTS

Our goal is to characterize quantities that describe biomolecular dynamics at the data-acquisition timescales of conventional single focus setup in order to obtain diffusion coefficient estimates.

Our overall input consists of: i) the measured photon inter-arrival times $\boldsymbol{\Delta t} = (\Delta t_1, \Delta t_2, ..., \Delta t_{K-1})$, where $\Delta t_{k-1} = t_k - t_{k-1}$ with t_k denoting the arrival time of the kth photon; ii) the geometry of the illuminated volume specified through a characteristic PSF; and iii) the background photon emission rate. The latter are determined through a pre-calibration step [12].

In order to estimate the biomolecules' diffusion coefficient, D, we also estimate intermediate quantities (namely, particle photon emission rates, biomolecule positions over time and biomolecule numbers) detailed in the methods section. These intermediate quantities demand that we use Bayesian nonparametrics to determine quantities that *a priori* may be arbitrarily large such as the number of the diffusing biomolecules contributing photons.

Within the Bayesian paradigm [55, 98], our estimates take the form of posterior probability distributions over unknown quantities. These distributions combine parameter values, probabilistic relations among different parameters, as well as the associated uncertainties. To quantify this uncertainty, we compute a posterior variance and use this variance to construct error-bars (i.e., credible intervals). According to the common statistical interpretation [34, 98], the sharper the posterior, the more conclusive (and certain) the estimate.

Here, we first validate our method on synthetic data where ground truth is readily available. We then test our method on experimental data collected in two labs utilizing different FCS setups. For the latter cases, we compare our analyses to the results obtained from autocorrelative methods used in FCS.

A. Method Validation using Simulated Data

To demonstrate the robustness of our approach, we simulate raw traces under a broad range of: i) trace lengths, Fig. (4); ii) concentrations of labeled biomolecules, Fig. (5); iii) diffusion coefficients, Fig. (6); and iv) particle photon emission rates, Fig. (7). The parameters not varied are held fixed at the following values: diffusion coefficient of 1 $\mu m^2/s$ which is typical of slower *in vivo* conditions [5, 63, 81, 96], particle photon emission rates of 4×10^4 photons/s [57, 76], and 4 as the number of labeled biomolecules contributing to the trace. We chose a small number of biomolecules (as opposed to a larger number of biomolecules) as this scenario presents the greatest analysis challenge (as very few photons, and thus thus little information, is gathered). It is important to emphasize here that the particle photon emission rate is defined here at the center of the confocal volume (which is the maximum number of emitted photons per label emitted from a single fluorophore that happen to be located at the center of the confocal volume). For more detail please see the Supplementary Information (SI).

A critical and recurring point throughout this section will be that the traces we analyze are shorter than those that could be meaningfully analyzed using FCS as illustrated in Fig. (1). While we focus on the diffusion coefficient estimation here, we note that our framework supports more detailed parameter estimation. In particular, in the SI we illustrate simultaneous estimation of particle photon emission rates; locations of biomolecules relative to the confocal volume center; as well as numbers of biomolecules within given regions around the confocal volume center.

1. *Trace Length*

We evaluate the robustness of our method with respect to the length of the trace (i.e., the total number of photon arrivals) at fixed number of biomolecules, diffusion coefficient, and particle photon emission rates. The first important finding is that, for the values of parameters selected, we need 2 orders of magnitude less data than FCS; see Fig. (1C). For instance, to obtain an estimate of the diffusion coefficient within 10% of the correct result, we require $\approx 10^3$ photons (directly emitted from the labeled

biomolecule), while FCS requires $\approx 10^5$ photons. To determine this percentile we chose the mean value of the diffusion coefficient posterior, and measure the percentage difference of this mean to the ground truth known for these synthetic traces.

In general, the difference in the photon numbers demanded by our method and traditional FCS analysis depend on a broad range of experimental parameter settings. This is the reason, we explore different settings–holding all other settings fixed–in subsequent subsections as well as the SI.

Another important concept–illustrated in Fig. (1C) and Fig. (4) that will keep re-appearing in subsequent sections–is the concept of a photon as a unit of information. The more photons we have, the sharper our diffusion coefficient estimates. This is true, as we see in Fig. (1C) and Fig. (4), for increasing trace length. Similarly, as we will see in subsequent subsections, we also collect more photons as we increase the concentration of labeled biomolecules (and thus the number of biomolecules contributing photons to the trace), increase the particle photon emission rates of biomolecular labels (or dyes in the case of free dye experiments), or decrease diffusion coefficients of biomolecules. In the latter case, slower diffusion coefficients provides more time for each biomolecule to traverse the illuminated region.

2. *Labeled Biomolecule Concentration*

To test the robustness of our method under different concentrations of labeled biomolecules at fixed diffusion coefficient, and particle photon emission rates, we simulate diffusing biomolecules with average concentrations of 10 biomolecules/μm^3 (Fig. (5A, B)), 4 biomolecules/μm^3 (Fig. (5C, D)), all the way down to 1 biomolecule/μm^3 (Fig. (5E, F)), diffusing at 1 μm^2/s for a total time 30 ms. The particle photon emission rates per label of labeled biomolecules and background are taken to be 4×10^4 photons/s and 10^3 photons/s respectively, which are typical of confocal microscope [76]. Our method is general and can readily treat arbitrary confocal volume geometries such as a Lorentzians [10] or Airy patterns [105] though, for simplicity, in generating synthetic data we use a 3D Gaussian volume of size ω_{xy}=0.3 μm and ω_z=1.5 μm [54]). Fig. (5) summarizes our results and suggests that posteriors over diffusion coefficients are broader–and thus the accuracy with which we can pinpoint the diffusion coefficient drops–when the concentration of labeled biomolecules is lower. Intuitively, we expect this result as fewer biomolecules within the confocal volume provide fewer photons and each photon carries with it information that helps refine our diffusion coefficient estimate. In the opposite extreme, when biomolecular numbers are high and detectors themselves are saturated, both the experimental setup and one's choice of single-photon analysis methods are inappropriate.

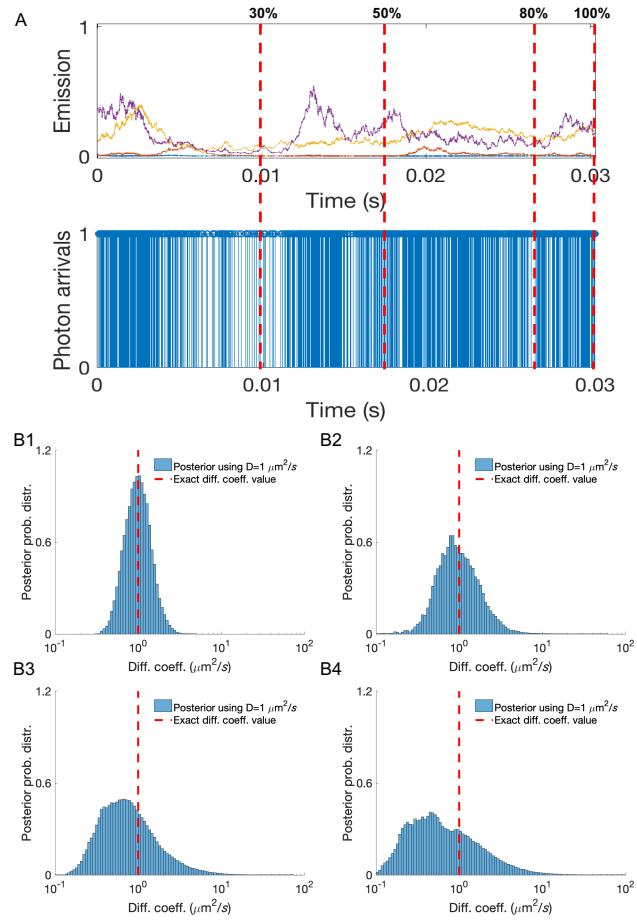

FIG. 4. **The larger trace length provides more photons per unit time and thus sharper diffusion coefficient estimates**. (A) The upper panel shows the normalized instantaneous photon emission rates of all biomolecules which depend on the location of the biomolecules with respect to the center of the confocal volume (Eq. (3)) and the bottom panel is its related photon arrival trace that comes from summing the emission rates over all biomolecules plus the background emission. This trace is acquired for a total time of 30 ms (with a total of about 10^3 photon arrivals) and generated using a diffusion coefficient $1\mu m^2/s$ with background and labeled particle photon emission rates of 10^3 photons/s and 4×10^4 photons/s respectively with about 1000 photons. The 80% dash line shows 80% of the original trace with about 800 photons. Similarly for the 50% and 30% dashed lines which include 500 and 300 photons respectively to their left. (B1-B4) Correspond to posterior probability distributions drawn from traces of differing length. The horizontal axis is shown in logarithmic scale for convenience.

3. *Diffusion Coefficients*

We repeat the simulations of the previous subsection to demonstrate, using synthetic data, the robustness of our method with respect to the diffusion coefficient magnitude; see Fig. (6) at fixed number of biomolecules, and particle photon emission rates. Intuitively–and again on

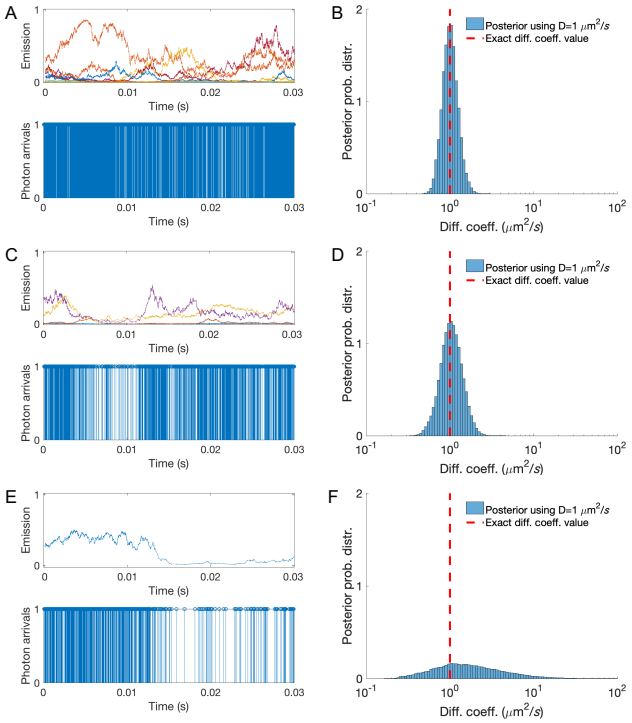

FIG. 5. **Higher molecular concentrations provide more photons per unit time and thus sharper diffusion coefficient estimates**. (A) The synthetic trace is acquired for a total time of 30 ms with a diffusion coefficient of $1\mu m^2/s$ and background and particle photon emission rates 10^3 photons/s and 4×10^4 photons/s respectively. The upper panel represents normalized instantaneous photon emission rates of all biomolecules which depend on the location of the biomolecules with respect to the center of the confocal volume, Eq. (3). The bottom panel is its related photon arrival trace that comes from the sum of emission rates over all biomolecules plus the background emission. The photon arrival trace is produced by 10 biomolecules. We then sum these traces. (B) Posterior probability distribution over the diffusion coefficient estimated from the trace in (A). (C) Synthetic trace produced by 4 biomolecules similar to panel (A). (D) Posterior probability distribution over the diffusion coefficient estimated from the trace in (C). (E) Synthetic trace produced by one biomolecule. (F) Posterior probability distribution over the diffusion coefficient estimated from the trace in (E).

the basis of the fact that photons carry information–we expect that faster moving species will give rise to broader posterior distributions as these species emit fewer photons, and thus provide less information, as they traverse the confocal volume.

4. *Particle Photon Emission Rates*

Fig. (7) illustrates the robustness of our method with respect to particle photon emission rates (i.e., set by the laser power used in the experimental setting or the choice of fluorescent label or dye) by fixing the number of biomolecules, diffusion coefficient (1 $\mu m^2/s$), and background emission, 10^3 photons/s. To accomplish this, we simulate increasingly dimmer biomolecules until the biomolecule signature is effectively lost as compared to the background. As expected, weaker traces lead to poor estimation and broader posterior estimates over diffusion coefficients since these traces are associated with greater uncertainty.

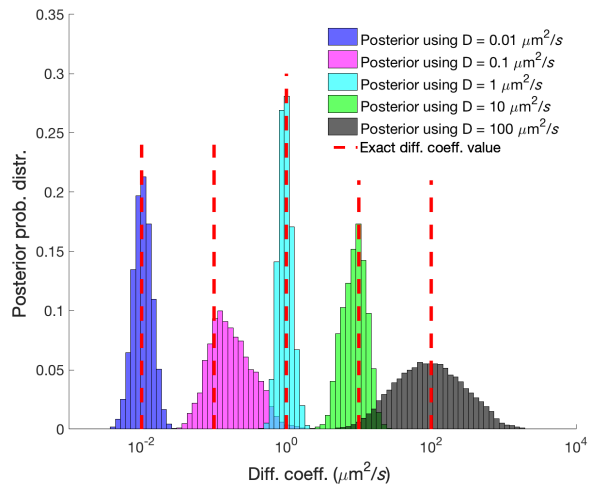

FIG. 6. **Smaller diffusion concentrations provide more photons per unit time and thus sharper diffusion coefficient estimates**. The effects of different diffusion coefficients (D= 0.01, 0.1, 1, 10, and 100 $\mu m^2/s$). Posterior probability distributions drawn from traces produced from biomolecules of differing diffusion coefficient. For sake of clarity, the horizontal axis is shown in logarithmic scale. Posterior probability distributions drawn from traces of the same length (30 ms about 1500 photons) for D= 0.01, 0.1, 1, and 10, $\mu m^2/s$ and for D= 100 $\mu m^2/s$. We used 50 ms or about 3000 photons for the fastest diffusion coefficient as we need longer traces to collect enough photons and gather the information needed to construct the posterior. We used background and particle photon emission rates per label of 10^3 photons/s and 4×10^4 photons/s, respectively.

B. Estimation of Physical Parameters from Experimental Data

To evaluate our approach on real data, we used experimental data collected under a broad range of conditions. That is, we used measurements from two different experimental setups and different fluorescent biomolecules, namely Cy3 and 5-TAMRA dyes. Additional differences between the setups include different numerical apertures (NA), laser powers, and overall detection instrumentation as detailed in the methods section.

Figs. (8)-(10) were collected using the Cy3 dye and these results were used to benchmark the robustness of our method on dye concentration, diffusion coefficients, and laser power. The last figure, Fig. (11), was collected

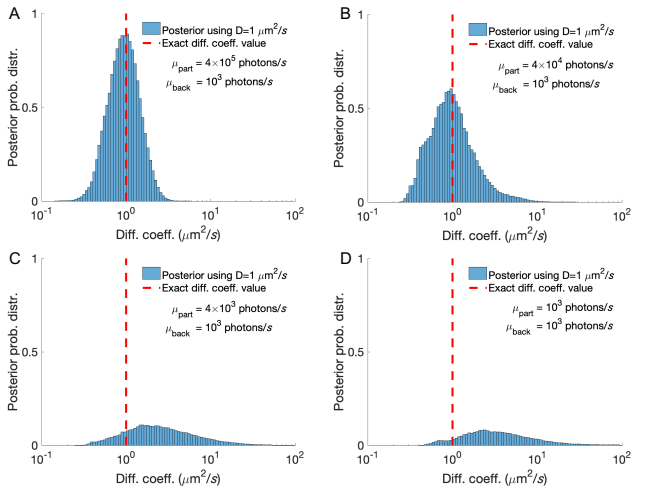

FIG. 7. **Greater particle photon emission rates provide more photons per unit time and thus sharper diffusion coefficient estimates**. Traces produced by the same molecular trajectories under differing particle photon emission rates per label (4×10^5, 4×10^4, 4×10^3, 10^3 photons/s) with different number of photons with the same diffusion coefficient $1\mu m^2/s$ and background photon emission rate 10^3 photons/s. In the generation of these traces, the background emission rate is kept fixed (with the most difficult case, (D), coinciding with identical background and particle photon emission rates). (A-D) Posterior probability distributions and exact values of diffusion coefficients are obtained from the corresponding traces. For more details about the trace see the SI.

using a 5-TAMRA dye in order to test the robustness of our method on a different fluorophore.

1. *Benchmarking on experimental data using Cy3*

We began by verifying our method on mixtures of water and glycerol. In spite of the fact that we only utilize short segments in our analyses, the collected traces are long enough (≈5 min each) to be meaningfully analyzed by traditional auto-correlative analysis used in FCS. The result of the analysis of the full trace by FCS yielded a diffusion coefficient that we treated as an effective ground truth. We can then ask how long of a trace our method requires, as compared to FCS, in order for our diffusion coefficient estimate to converge to this ground truth.

The latter strategy addresses the following complication: we anticipate that the PSF may be distorted from the idealized shape assumed especially with increasing amounts of glycerol [36]. However, the same (possibly incorrect) PSF is assumed in both FCS and our method in order to compare both methods head-to-head. Thus, concretely, we will be asking: how many photons do we need to converge to the same result as FCS (irrespective of whether the FCS result is affected by PSF distortion artifacts)?

In part, we also do this as auto-correlative analysis in FCS cannot easily treat complex PSF shapes. Indeed, the fluorescence intensity time auto-correlation function loses its analytic form otherwise afforded by assumptions of PSF Gaussianity. We add that while we do not here learn the PSF shape using our method (instead, we assume its shape), our method can naturally treat any PSF shape provided it is known, i.e., has been pre-calibrated (see SI section 1).

Data were obtained under a range of conditions to test our method, namely different: i) dye concentrations, Fig. (8); ii) diffusion coefficients, Fig. (9); and iii) laser power, Fig. (10). As before, longer traces, higher concentrations, lower D's, and higher laser power result, on average, in sharper estimates with results on diffusion coefficient estimates still converging with at least 2 orders of magnitude less data than FCS for equal accuracy in Figs. (8), (9), and Fig. (10) respectively. We mention "on average" as individual traces are stochastic. Thus, some traces with higher concentrations of labeled biomolecules, say, may happen to have fewer biomolecules contribute photons to the traces than experiments with lower concentrations.

Fig. (8) recapitulates our expectations derived from the synthetic data shown earlier (Fig. (5)), when dye concentrations are low yielding wider posterior for our diffusion coefficient and correspondingly sharper posteriors for the higher concentration. Here, similarly to Fig. (1) we compare our method's diffusion coefficient estimate to FCS as a function of the number of photons used in the analysis, Fig. (8A) and Fig. (8B), both in good agreement with FCS estimates, produced by the entire traces (i.e., 1000× longer).

Similar to the analysis of the synthetic data, by comparing different diffusion coefficients, the slower a diffusing biomolecule is, the more time it spends within the confocal volume, the more photons are collected providing us with a sharper posterior estimate of its diffusion coefficient (see Fig. (9)).

Similarly to the synthetic data shown earlier (Fig. (7)), Fig. (10) now considers the robustness of our method to lower laser power which, as expected, yields a wider posterior for our diffusion coefficient and correspondingly sharper posteriors for higher laser power. Here, we compare our method's diffusion coefficient estimate to FCS as a function of the number of photons used in the analysis, Fig. (10A) and Fig. (10B), both in good agreement with FCS estimates, produced from the entire trace.

2. *Benchmarking on experimental data using 5-TAMRA*

Here we switch to a different dye, different setup and acquisition electronics as detailed in the Methods section. Our sample now contains 20 nM of 5-TAMRA dissolved in water. We evaluate the diffusion coefficients versus the value obtained from both FCS and NMR [35], see Fig. (11). Although we used short segment for the anal-

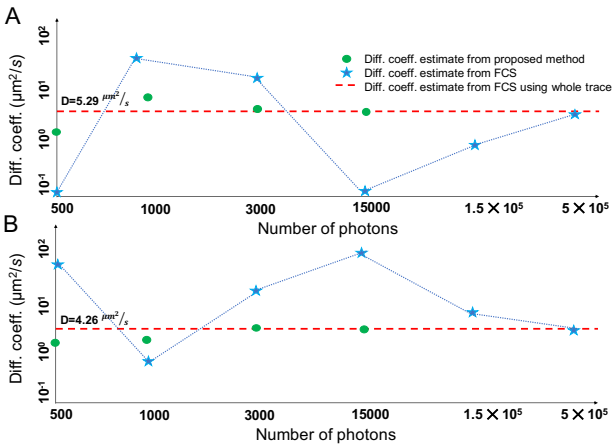

FIG. 8. **Using higher molecular concentrations in experimental traces (with Cy3 setup) provides more photons per unit time resulting in sharper diffusion coefficient estimates**. Experimental fluorescent intensity traces with a low (100 pM) (A) and high (1 nM) (B) concentration of dye biomolecules and 75% Glycerol at a fixed laser power of $100\mu W$. Similarly to Fig. (1), we compare our method's diffusion coefficient estimate (circle green dots) to FCS (blue stars) as a function of the number of photons used in the analysis. The red dash line is the FCS estimate produced from the entire 5 minute trace containing $\sim 3 \times 10^6$ photon arrivals. This red dashed line is treated as the ground truth.

ysis, we compare our results to analyses on much longer (≈10 min) traces from FCS.

IV. DISCUSSION

The photon is the basic unit of information in all spectroscopic and imaging applications [68]. Our method takes a Bayesian nonparametric approach to tackling single photon arrival data to learn dynamical quantities from as few as hundreds to thousands of photons from confocal imaging data. This is by contrast to conventional auto-correlative methods used in FCS [27, 64, 78, 95] that require dramatically more data, i.e., datasets several orders of magnitude larger in either total duration or total number of photon arrivals, to characterize dynamical quantities with similar accuracy. These quantities include diffusion coefficients, instantaneous number of biomolecules, the position of biomolecules within the illuminated confocal volume, and particle photon emission rates for each biomolecular label.

There have been partial solutions to the challenge of interpreting data at the single photon level often outside FCS applications. Indeed, existing methods make assumptions that would render them inapplicable to diffusion in an inhomogenesouly illuminated volume. For example, they assume uniform illumination [38, 76], bin the data and thereby reduce temporal resolution to exploit existing mathematical frameworks such as the Hidden Markov model [2, 16, 39, 70, 97], or focus on immobile biomolecules [23, 24, 37, 39]. As a result, correlative methods continue to dominate confocal data analysis as they have for the past 40 years [52].

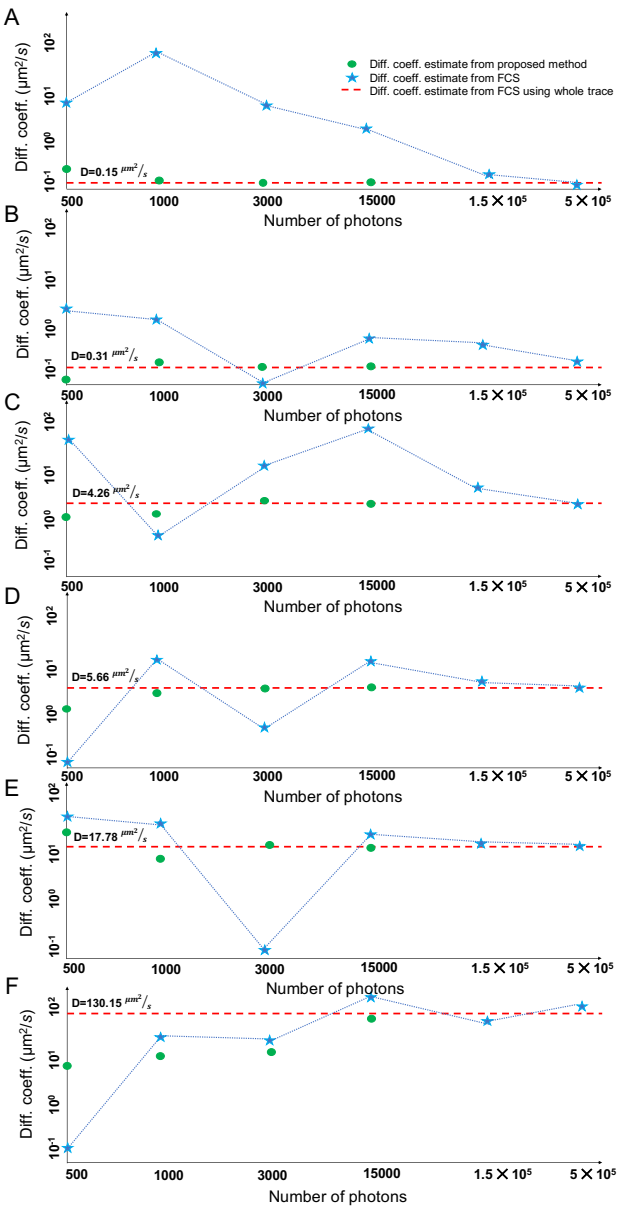

FIG. 9. **Smaller diffusion coefficients in experimental traces (using Cy3 setup) with higher percentage of Glycerol provide more photons per unit time and sharper diffusion coefficient estimates**. Here we used fixed concentrations of dye molecules (1 nM) and fixed laser power ($100\mu W$). We used traces with 99% Glycerol (0.15 $\mu m^2/s$) (A), 94% Glycerol (0.30 $\mu m^2/s$) (B), 75% Glycerol (4.26 $\mu m^2/s$) (C), 67% Glycerol (5.66 $\mu m^2/s$) (D), 50% Glycerol (17.78 $\mu m^2/s$) (E), 0% Glycerol (130.64 $\mu m^2/s$) (F). See Fig.(8) for more details.

To take full advantage of the single photon data–

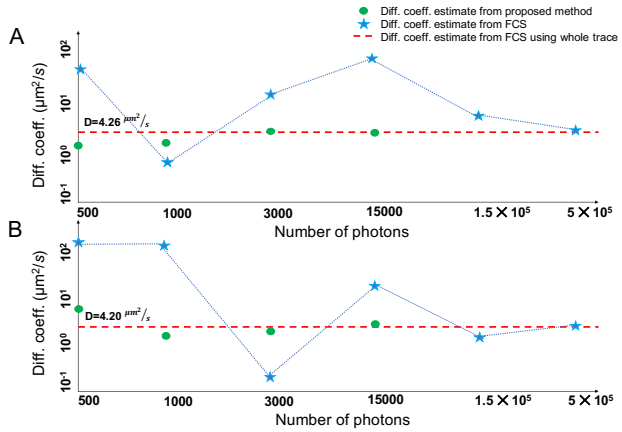

FIG. 10. **Higher laser power in experimental trace (with Cy3 setup) yields more photons per unit time and thus sharper diffusion coefficient estimates**. Experimental traces obtained under high ($100\mu W$) (A) and low ($25\mu W$) (B) laser power at fixed concentration (1 nM) and 75% Glycerol. See Fig.(8) for more details.

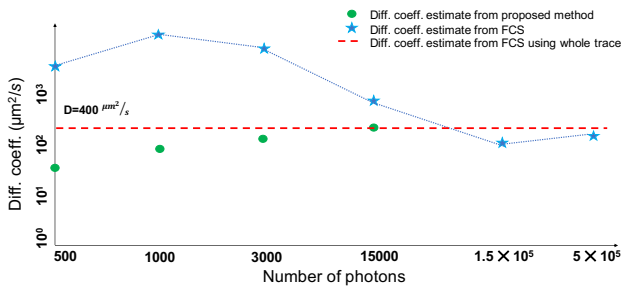

FIG. 11. **Diffusion coefficient estimates are obtained using 5-TAMRA dye**. Here we use 5-Carboxytetramethylrhodamine (5-TAMRA) at a fixed concentration (20 nM). Similarly to Fig. (1), we compare our method's diffusion coefficient estimate (circle green dots) to FCS (blue stars) as a function of the number of photons used in the analysis. For sake of comparison, the diffusion coefficient above was estimated from FCS (red dash line) using the entire trace ($\approx$ 10 min with 6×10^6 photons). For more details on how the FCS analysis is achieved see the SI.

and the inherent non-stationarity between photon arrivals both due to biomolecular diffusion in an inhomogeneously illuminated volume and the stochastic number of biomolecules contributing photons to the trace–new Mathematics are required. In particular, analyzing data derived from mobile biomolecules within an illuminated confocal region breaks down the perennial parametric Bayesian paradigm that has been the workhorse of biophysical data analysis [16, 44, 55, 60, 70, 92, 96]. We argue here that BNPs–which provide principled extensions of Bayesian logic [31, 93]–show promise in Biophysics [46, 55, 87, 88, 90, 92] and give us a working solution to prior parametric challenges.

Within BNPs, the mathematical device on which we most heavily rely, the Beta-Bernoulli process, is only half a decade old. Our new tools open up the possibility to explore at the single photon level non-equilibrium processes resolved on fast timescales [3, 69], say ms, that have been the focus of recent attention.

In addition, armed with a rigorous framework, it is now possible to extend the proof-of-principle framework we put forward to treat different effects that lie beyond the current scope of this work. In particular, we can think of extending our framework to treat multiple colors [22], triplet effects, complex biomolecule photophysics [41] (such as biomolecular blinking [89, 104] and photobleaching [56, 91]), more complex biomolecule motion models [103] other than free diffusion [50], complex distorted PSF models [29], or even incorporate chemical reactions among the biomolecules [8, 100].

ACKNOWLEDGEMENTS

S.P. acknowledges support from the NIH NIGMS (R01GM130745-01). S.S. acknowledges support from the NIH NIGMS (R01GM121885).

AUTHOR CONTRIBUTIONS

MT analyzed data and developed analysis software; MT, SJ, IS developed computational tools; OS, SS, BD, ML contributed experimental data; MT, SJ, IS, SP conceived research; SP oversaw all aspects of the projects.

SUPPLEMENTARY MATERIALS

In this supplement, we present additional analyses and technical details expanding upon the material presented in the main text. These include: i) additional analysis of synthetic and experimental traces that include the estimation of diffusion coefficient, average photon emission rates and the estimation of biomolecular locations/concentrations; ii) additional details on the theoretical approaches used; and iii) a complete description of the inference framework developed that includes choices for prior probability distributions and a computational implementation.

Additional results

Analysis of additional simulated data

In the main text we focused on the estimation of: diffusion coefficients, D, with values $\approx 1\mu\text{m}^2/\text{s}$ which are typical of slower *in vivo* applications [5, 63, 81, 96],

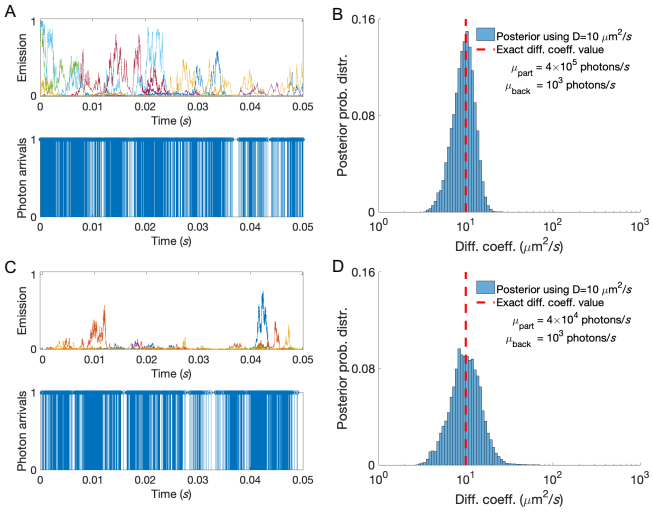

FIG. 12. **Estimation of diffusion coefficient with different particle photon emission rates. Larger particle photon emission rates provide greater photon numbers per unit time and thus better diffusion coefficient estimates**. (A) The upper panel shows the normalized instantaneous photon emission rate of all biomolecules which depend on the location of the biomolecules with respect to the center of confocal volume (Eq. (18)). The bottom panel illustrates the upper panel's associated photon arrival trace that comes from summing all output over all biomolecules in addition to background photons. This trace is acquired for a total time of $50ms$ with the size of the confocal volume of 0.3 μm along the x and y directions and 1.5 μm along the z direction, and generated using 10 biomolecules, a particle diffusion coefficient of $10\mu m^2/s$ and background and particle photon emission rates 10^3 photons/s and 4×10^5 photons/s, respectively. For more information about the values of all parameters see Tables (III) and (IV). (B) Posterior probability distribution over the diffusion coefficient estimated from the trace. (C) The trace is acquired just as before for the same length of time, $50ms$, but with lower particle photon emission rate 4×10^4 photons/s (background fixed at 10^3 photons/s). (D) Posterior probability distribution over the diffusion coefficient estimated from the trace. Comparing (B) and (D) suggests our current method works with different particle photon emission rates. The higher the particle photon emission rate, the more photons we collect and the better the estimate we obtain (i.e., the sharper our posteriors).

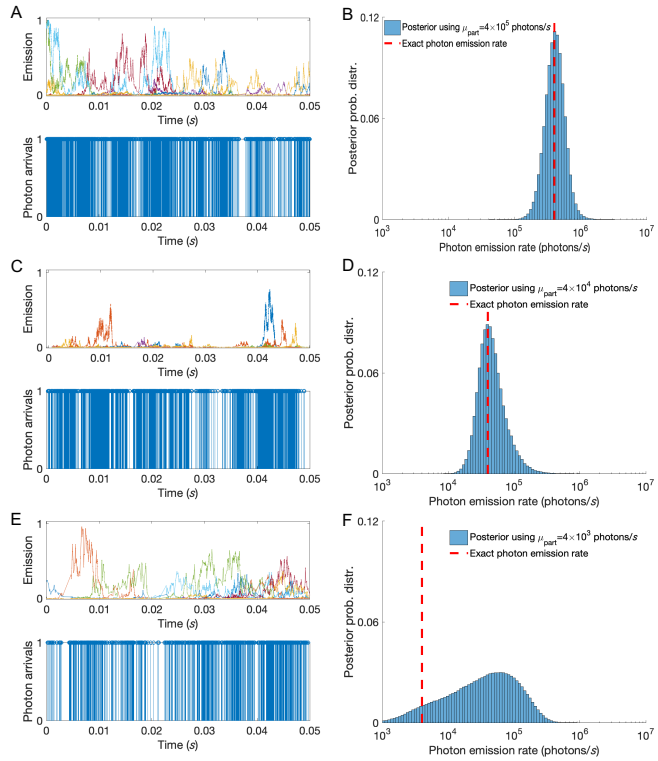

FIG. 13. **Estimation of the particle photon emission rate. Higher particle photon emission rates provide more photons per unit time and thus better emission rate estimates**. Traces produced by the same biomolecular trajectories under differing particle photon emission rates (4×10^5 (A), 4×10^4 (C), 4×10^3 (E) photons/s) with the same diffusion coefficient $10\mu m^2/s$ and background photon emission rate of 10^3 photons/s. The size of the confocal volume considered is 0.3 μm along the x and y directions and 1.5 μm along the z direction, and generated using 10 biomolecules. The upper panel shows the normalized instantaneous photon emission rates of all biomolecules which depend on the location of the biomolecules with respect to the center of confocal volume (Eq. (18)) and the bottom panel illustrates the upper panel's associated photon arrival trace that comes from summing all output over all biomolecules in addition to background photons. (B-D-F) Posterior probability distributions and exact values of particle photon emission rates obtained from the corresponding traces. Comparing these posterior shows the higher the particle photon emission rate, the more photons we collect and the better estimates we obtain.

biomolecule photon emission rates of $\approx 4\times10^4$ photons/s [57, 76], and 4 biomolecules typically emitting photons over the course of a time trace. Here, we explore broader parameter ranges.

Analysis of additional Experimental data

Next, we used our method on real traces derived from a single focus confocal setup. Here, we used measurements from two different experimental setups and different fluorescent biomolecules, namely Cy3 and 5-TAMRA dyes. We used two separate experimental datasets: Fig. (15) was a result using Cy3 dye to benchmark the diffusion coefficients and particle photon emission rate; Fig. (16) was using a different dye, 5-TAMRA dye, to evaluate the approach with different diffusion coefficients, and particle photon emission rate, with different experimental setup. In the Methods section of the main text we have provided details of each setup. Briefly,the differences between these two setups are summarized in numerical aperture (NA), laser power, photon emission rate of biomolecule, and type of dye which used.

Below, we illustrate additional results showing the es-

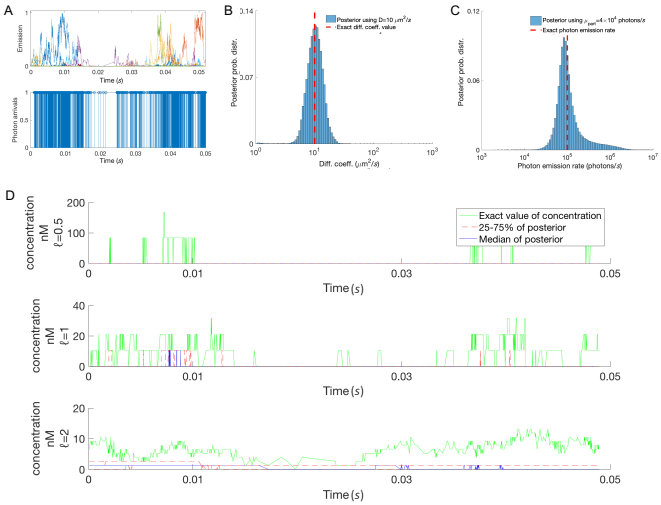

FIG. 14. **Estimating biomolecule locations/concentrations**. (A) Synthetic trace produced with a particle photon emission rate of 4×10^4 photons/s and a background photon emission rate of 10^3 photons/s, diffusion coefficient of 10 μm^2/s and concentration of 10 biomolecules/μm^3. In generating these traces, the size of the confocal volume considered is 0.3 μm along the x and y directions and 1.5 μm along the z direction. For more information about the values of all parameters see Tables (III) and (IV). (B) Posterior probability distribution over the diffusion coefficient estimated from the trace. (C) Posterior probability distribution over the photon emission rate estimated from the trace. (D) Concentration of biomolecules estimated from the trace in (A) corresponding to normalized distances from the confocal volume center of $\ell = 0.5$ (upper panel), 1 (middle panel), 2 (bottom panel). The exact concentration is shown by the green lines, the 50% quantile of the posterior over the concentration is shown by the blue lines, and the area between 25% and 75% quantiles of the posterior over the concentration is highlighted in red. For details of the definition of concentration c_k^ℓ and the normalized distance ℓ, see Eq. (20), below.

timation of diffusion coefficient, particle photon emission rate and a comparison with conventional FCS analyses.

Detailed methods description

Brief description of fluorescence correlation spectroscopy (FCS)

In FCS the primary quantity of interest are spontaneously fluctuating fluorescence intensities [26, 83]. Correlations in fluorescence intensities are used to determine physical parameters such as local concentrations, diffusion coefficients or characteristic rate constants of inter- or intramolecular reactions.

The normalized time autocorrelation function of the

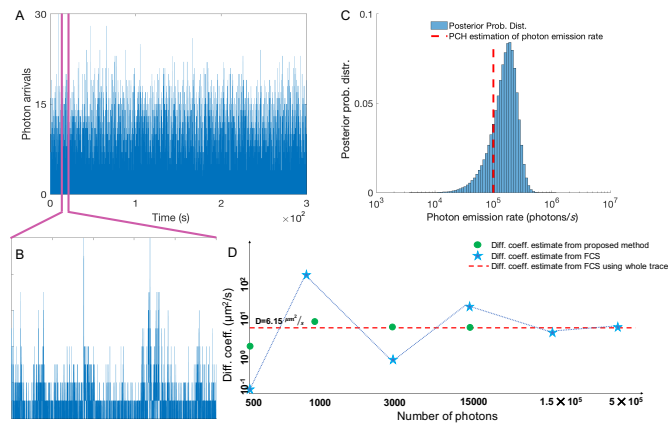

FIG. 15. **Estimation of diffusion coefficient, and particle photon emission rate for Cy3**. (A) Whole trace which was used to determine the value of the diffusion coefficient using FCS. The trace was generated using a concentration of 1 nM of Cy3 in a mixture of 61% glycerol at fixed laser power of 100 μW. For sake of comparison, the diffusion coefficient above estimated by FCS, generated using full traces 5 mins long (about 3×10^6 photons), are highlighted with a dashed line. For all estimates, the background emission rate is known from calibration and fixed at 600 photons/s. For more information about the values of all parameters see Table (IV). (B) The selected portion of the experimental trace (binned photon arrivals) containing about 3000 photons. (C) Posterior probability distributions and the value (red dash line) of particle photon emission rates determined by using the photon counting histogram (PCH) method. (D) Comparison between the diffusion coefficient estimate using our current approach (circle green dots) and FCS (blue stars) as a function of the number of photons used in the analysis. The red dash line is the FCS estimate produced from the entire 5 minute traces (3×10^6 photon arrivals).

fluorescence intensity is defined as:

$$G(\tau) = \frac{\langle I(t)I(t+\tau)\rangle}{\langle I(t)\rangle^2} \tag{10}$$

where $I(t)$ is the fluorescence intensity. For one freely diffusing species of biomolecules, this autocorrelation is

$$G(\tau) = \frac{1}{\langle N\rangle}\frac{1}{1+\frac{4D\tau}{\omega_{xy}^2}}\frac{1}{\sqrt{1+\frac{4D\tau}{\omega_z^2}}} \tag{11}$$

where, D is the diffusion coefficient, ω_{xy} and ω_z are the confocal volume axes along the x, y and z directions. Here, the first term of Eq. (11) is the inverse of the average number of biomolecule in the confocal volume. Therefore, by knowing the dimensions ω_{xy} and ω_z from calibration measurements, the local concentration of fluorescent biomolecules can be determined. For details on correlative analysis are contained in the cited literature [14, 26, 27, 32, 64, 83].

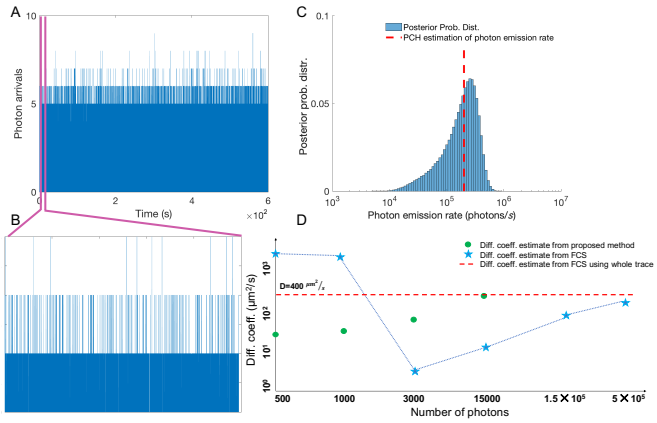

FIG. 16. **Estimation of diffusion coefficient, particle photon emission rate, and number of active biomolecules in 5-TAMRA setup**. (A) Whole trace which was used to determine the value of the diffusion coefficient using FCS. The trace was generated using 20 nM 5-Carboxytetramethylrhodamine (5-TAMRA). For sake of comparison here we use the diffusion coefficient above estimated by FCS (over the entire 10 min trace with about 6×10^6 photons) highlighted with a dashed line. Across all estimates, the background emission rate is known from calibration and fixed at 300 photons/s. For more information about the values of all parameters see Table (IV). (B) The selected portion of the experimental trace (binned photon arrivals) using about 8000 photons. (C) Posterior probability distributions and the value (red dash line) of particle photon emission rates determined by using the PCH method. (D) Comparison between the diffusion coefficient estimate using our method (circle green dots) and FCS (blue stars) as a function of the number of photons used in the analysis. The values of diffusion coefficients obtained from the entire trace using FCS are shown with a red dash line.

Representation of biomolecule diffusive motion

For a biomolecule diffusing along one direction, the probability distribution $p(x,t)$ of its position x at time t satisfies the diffusion equation [51]

$$\frac{\partial p}{\partial t} = D\frac{\partial^2 p}{\partial x^2} \tag{12}$$

where D is the diffusion coefficient of the biomolecule. We can solve this equation to obtain $p(x,t)$ for any later time t by assuming that the biomolecule is located at x_{k-1} at time t_{k-1}, i.e., using the initial condition $p(x,t_{k-1}) = \delta(x - x_{k-1})$, and a free space boundary, i.e., $\lim_{x\to\pm\infty} p(x,t) = 0$. The solution is

$$p(x,t) = \frac{\exp\left(-\frac{(x-x_{k-1})^2}{4(t-t_{k-1})D}\right)}{\sqrt{4\pi(t-t_{k-1})D}} \tag{13}$$

which is the probability density of a normal random variable with mean x_{k-1} and variance $2(t-t_{k-1})D$; for example, see Table II. At time $t = t_k$, we therefore have

$$x_k|x_{k-1} \sim \text{Normal}\left(x_{k-1}, 2\Delta t_{k-1}D\right) \tag{14}$$

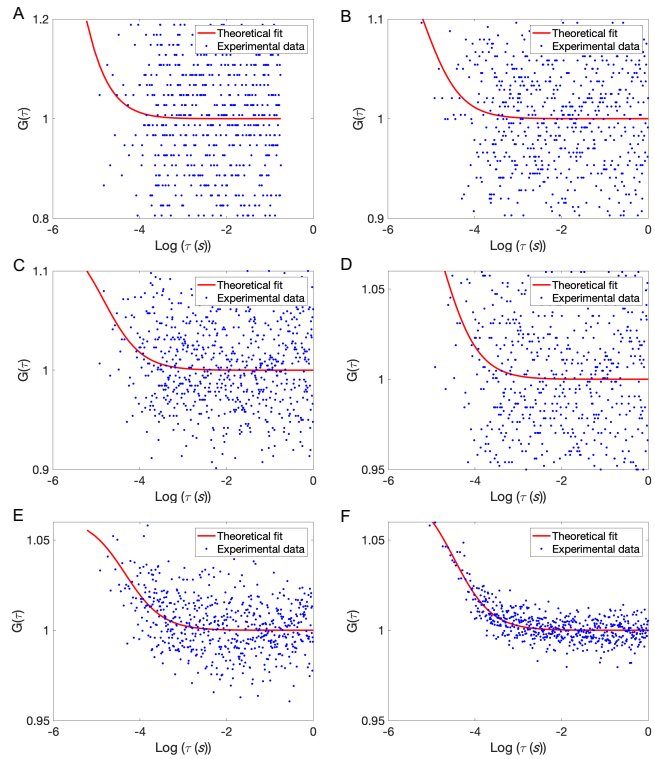

FIG. 17. **Auto-correlation curves with different numbers of photons in sample 5-TAMRA experimental data illustrating how poorly auto-correlative methods work with limited data on the order of the amount of data used in our method**. Auto-correlation curves, $G(\tau)$, of sample experimental trace with 500 photons (A), 1000 photons (B), 3000 photons (C), 15000 photons (D), 1.5×10^5 photons (E), and 1.5×10^6 photons (F). Normally, in FCS analysis, much longer traces would be used to generate much smoother $G(\tau)$'s that would then be fitted to determine diffusion coefficients. To create these auto-correlation curves, we used Eq. (11) with a confocal volume size of $0.221\mu m$ along the x and y direction and $3.90\mu m$ along the z direction.

where $\Delta t_{k-1} = t_k - t_{k-1}$ in accordance with the notation in remaining on this study.

Similarly, solving the diffusion equation for biomolecules following isotropic diffusion in free space along all three Cartesian directions we obtain

$$x_k|x_{k-1} \sim \text{Normal}\left(x_{k-1}, 2\Delta t_{k-1}D\right) \tag{15}$$
$$y_k|y_{k-1} \sim \text{Normal}\left(y_{k-1}, 2\Delta t_{k-1}D\right) \tag{16}$$
$$z_k|z_{k-1} \sim \text{Normal}\left(z_{k-1}, 2\Delta t_{k-1}D\right) \tag{17}$$

that constitute the biomolecular motion model used throughout this study.

Explanation of data simulation

To generate traces imitating raw data generated from a realistic confocal setup, we simulate biomolecules mov-

ing through a three dimensional (3D) illuminated volume. The number of moving biomolecules, N, is predefined in each simulation. We apply periodic boundaries to our volume of L_{xy} and L_z parallel to the focal plane and optical axis, respectively, to keep a relatively stable concentration of biomolecules near the confocal volume.

We denote the locations of the biomolecules as x_k^n, y_k^n and z_k^n, where k labels time levels and $n = 1, 2, \ldots$ labels biomolecules. The total trace duration $T_{total} = t_K - t_1$, is predefined. The inter-arrival times or time intervals between successive assessments (recorded photons) $\Delta t_{k-1} = t_k - t_{k-1}$, are generated through pseudo-random computer simulations and recorded for subsequent analysis.

The locations of the biomolecules at the first assessment x_1^n, y_1^n and z_1^n are randomly sampled from the uniform distribution with limits equal to the boundaries $\pm L_{xy}$ and $\pm L_z$ of our prescribed simulation region. Subsequent locations are generated according to the diffusion model described above under a predefined diffusion coefficient D.

We obtain photon inter-arrival times, $\boldsymbol{\Delta t} = (\Delta t_1, \Delta t_2, \ldots, \Delta t_{K-1})$, by simulating exponential random variables of rate μ_k. For independent background and particle photon emission rates, the corresponding exponential emission mean rates μ_k depend on a Gaussian point spread function (PSF) as follows

$$\mu_k = \mu_{back} + \sum_n \mu_k^n \tag{18}$$

where $\mu_k^n = \mu_{part} \exp\left(-2\frac{(x_k^n)^2+(y_k^n)^2}{\omega_{xy}^2} - 2\frac{(z_k^n)^2}{\omega_z^2}\right)$ and both background, μ_{back}, and the particle photon emission rate of detected photons for a single biomolecule, μ_{part}, are predefined. Here, ω_{xy} and ω_z are the semi-minor and semi-major axes lateral and parallel to the optical axis [11, 36]. Similarly, the dimensions of the PSF, ω_{xy} and ω_z, are also prescribed. To avoid artifacts induced by the periodic boundaries, we ensure that $L_{xy} \gg \omega_{xy}$ and $L_z \gg \omega_z$.

Definition of normalized distance and biomolecule concentration

To estimate the diffusion coefficient, as we point out in the main text, we need to estimate the positions of the biomolecules with respect to the center of the confocal volume. Therefore, we have to address problems associated with the symmetries of the confocal PSF with respect to rotations around the optical axis or the focal plane. To bypass such difficulties, for a biomolecule at locations x_k^n, y_k^n, and z_k^n, we rely on the following normalized distance

$$d_k^n = \sqrt{\left(\frac{x_k^n}{\omega_{xy}}\right)^2 + \left(\frac{y_k^n}{\omega_{xy}}\right)^2 + \left(\frac{z_k^n}{\omega_z}\right)^2} \tag{19}$$

which is unaffected by the aforementioned symmetries.

Now, we define the concentration of biomolecules c_k^ℓ as the number of (active, i.e., photon emitting) biomolecules within the corresponding confocal volume, for a given ratio of normalized distance, d_k^n, and distance respect to effective volume, ℓ.

$$c_k^\ell = \frac{1}{V_\ell} \sum_n b^n H\left(1 - \frac{d_k^n}{\ell}\right) \tag{20}$$

where H is the Heaviside step function, b^n is the load of biomolecule n, and V_ℓ is the volume of the designated region of interest (ROI) which is given by

$$V_\ell = \pi^{\frac{3}{2}} \omega_{xy}^2 \omega_z \ell^3. \tag{21}$$

Calculating the average biomolecular photon emission rate

In this study the emission rate of detected photons for a single fluorophore at position x, y, z is used. This is formulated as the product

$$\mu(x,y,z) = \mu_0\ \varphi_d\ \varphi_{de}\ \varphi_f\ \sigma\ \mathrm{EXC}(x,y,z)\ \mathrm{CEF}(x,y,z). \tag{22}$$

Here, μ_0 and φ_d are the maximum excitation intensity and the efficiency of the photon collection at the center of the confocal volume respectively, φ_{de} is the efficiency of the detector, φ_f is the quantum efficiency of the fluorophore, σ is the absorption cross-section of the fluorophore, $\mathrm{EXC}(x,y,z)$ is the excitation profile and $\mathrm{CEF}(x,y,z)$ is the detection profile known as collection efficiency function that equals to the portion of the detected photons emitted by a point source [28].

Now, by revising Eq. (22) to the form of

$$\mu(x,y,z) = \mu_{part}\mathrm{PSF}(x,y,z) \tag{23}$$

where $\mu_{part} = \mu_0\ \varphi_d\ \varphi_{de}\ \varphi_f\ \sigma$ is called the brightness at the center of the confocal volume and $\mathrm{PSF}(x,y,z) = \mathrm{EXC}(x,y,z)\ \mathrm{CEF}(x,y,z)$ as the detection volume, we obtain $\mathrm{PSF}(x,y,z) = \exp\left(-2\frac{x^2+y^2}{\omega_{xy}^2} - 2\frac{z^2}{\omega_z^2}\right)$.

To relate our *single molecule* photon emission rate μ_{part} to the average photon count rate typically determined in *bulk* experiments, we compute the spatial average of $\mu(x,y,z)$ as follows

$$\langle \mu(x,y,z) \rangle = \mu_{part} \langle \mathrm{PSF}(x,y,z) \rangle$$

$$\langle \mu(x,y,z) \rangle = \mu_{part} \left\langle \exp\left(-2\frac{x^2+y^2}{\omega_{xy}^2} - 2\frac{z^2}{\omega_z^2}\right) \right\rangle$$

$$= \mu_{part} \frac{\int_{-\infty}^{+\infty}\int_{-\infty}^{+\infty}\int_{-\infty}^{+\infty} \exp\left(-2\frac{x^2}{\omega_{xy}^2} - 2\frac{y^2}{\omega_{xy}^2} - 2\frac{z^2}{\omega_z^2}\right) dxdydz}{V_{eff}}$$

$$= \mu_{part} \sqrt{\frac{\pi}{2}\omega_{xy}^2} \sqrt{\frac{\pi}{2}\omega_{xy}^2} \sqrt{\frac{\pi}{2}\omega_z^2} \frac{1}{V_{eff}} \tag{24}$$

where V_{eff} is the effective volume of our PSF [54, 79] and it is given by

$$V_{eff} = \pi^{\frac{3}{2}} \omega_{xy}^2 \omega_z. \tag{25}$$

As a result, our particle photon emission rate μ_{part} is related to $\langle \mu(x, y, z) \rangle$ according to

$$\mu_{part} = \sqrt{8}\ \langle \mu(x, y, z) \rangle. \tag{26}$$

Description of Wilson-Hiferty approximation

To perform the necessary computations of the next section, we use a Wilson-Hiferty transform [101] to approximate the probability density of exponential random variables. We use this approximation in section IV when we sample the locations of biomolecules within our overall Gibbs sampler.

To apply the Wilson-Hiferty approximation, first we transform our observation random variable Δt_k to a new random variable ρ, where $\rho = 2\mu_k \Delta t_k$. A change of variables, indicates that $\Delta t_k | \mu_k \sim \text{Exponential}(\mu_k)$ implies

$$\rho | \mu_k \sim \chi^2 (2) . \tag{27}$$

where $\chi^2(2)$ denotes the chi-square probability distribution with 2 degrees of freedom, see Table II. In other words, the above random variable ρ is a chi-square variate, $\rho \sim \chi^2(2)$.

Now, by applying another transformation, where $\xi = \sqrt[3]{\rho/2}$, according to [101], ξ follows an *approximately* normal probability distribution

$$\xi \sim \text{Normal} \left(\frac{8}{9}, \frac{1}{9} \right) . \tag{28}$$

So, by $\xi = \sqrt[3]{\rho/2}$ and $\rho = 2\mu_k \Delta t_k$, we conclude $\sqrt[3]{\Delta t_k} = \xi / \sqrt[3]{\mu_k}$. Therefore, since $\sqrt[3]{\Delta t_k} = \xi / \sqrt[3]{\mu_k}$, by transforming the distribution function in Eq. (28), we establish the approximation

$$P\left(\sqrt[3]{\Delta t_k} | \mu_k \right) = P\left(\xi = \sqrt[3]{\Delta t_k} \sqrt[3]{\mu_k} \right) \sqrt[3]{\mu_k} \tag{29}$$

$$\approx \sqrt[3]{\mu_k}\ \text{Normal} \left(\sqrt[3]{\Delta t_k} \sqrt[3]{\mu_k}; \frac{8}{9}, \frac{1}{9} \right)$$

$$= \text{Normal} \left(\sqrt[3]{\Delta t_k}; \frac{8}{9 \sqrt[3]{\mu_k}}, \left(\frac{1}{3 \sqrt[3]{\mu_k}} \right)^2 \right) . \tag{30}$$

Detailed description of the inference framework

Prior probability distributions

Within the Bayesian paradigm, all unknown model parameters need priors. These parameters are: the diffusion coefficient D; the particle photon emission rate μ_{part}; the initial biomolecule locations x_1^n,y_1^n,z_1^n; as well as the load prior weights q^n. Our priors are detailed below.

Prior on the diffusion coefficient

To make sure that the D sampled in our formulation attains only positive values, we place an Inverse-Gamma prior

$$D \sim \text{InvGamma} \left(\alpha_D, \beta_D \right) . \tag{31}$$

This prior is conjugate to the motion model which simplifies the computations shown below.

Priors on particle photon emission rate

To guarantee that μ_{part} sampled in our formulation also only attains positive values, we choose a Gamma prior

$$\mu_{part} \sim \text{Gamma} \left(\alpha_{part}, \beta_{part} \right) . \tag{32}$$

Due to the likelihood's dependence on μ_{part}, conjugate priors cannot be achieved for μ_{part}. So the above choice offers no computational advantage (see below) and could readily be replaced with more physically motivated choices if additional information on photon emission rates is available.

Priors on initial biomolecule locations

Because of the symmetries inherent to the confocal volume, e.g., a biomolecule at a location (x, y, z) gives rise to the same photon emission rate as a biomolecule at location, $(-x, -y, -z)$, we place priors on the initial locations that respect these symmetries. To eliminate further assumptions on our framework that may determine each biomolecule's position uniquely, but may limit the framework's scope to certain experimental setups, we apply a symmetric prior. Consequently, in our framework, at the beginning of the measuring period, biomolecules are equally likely to be located at any of the locations $(\pm x_1^n, \pm y_1^n, \pm z_1^n)$.

To simplify the computations, we place independent symmetric normal distributions, on each Cartesian coordinate of the model biomolecules

$$x_1^n \sim \text{SymNormal} \left(\mu_{xy}, \sigma_{xy}^2 \right) \tag{33}$$

$$y_1^n \sim \text{SymNormal} \left(\mu_{xy}, \sigma_{xy}^2 \right) \tag{34}$$

$$z_1^n \sim \text{SymNormal} \left(\mu_z, \sigma_z^2 \right) . \tag{35}$$

We emphasize that the above symmetric prior does not affect our estimation. According to the biomolecule's motion model we apply, no matter where biomolecules are initiated, eventually they may move freely and subsequently switch to a different octant if necessary. Our symmetric priors merely indicate that for each individual biomolecule trajectory considered, there are 7 other symmetric trajectories that are equally likely to have occurred.

Priors and hyperpriors for the loads

To simplify the computations described in the next section, we use a finite, but large, model population consisting of N biomolecules that contain active and inactive ones. These biomolecules are collectively indexed by $n = 1, 2, \ldots$. As explained in the main text, estimating how many biomolecules are actually warranted by the data analyzed is the same as estimating how many of those N biomolecules are active, i.e., $b^n = 1$, while the rest are inactive, i.e., $b^n = 0$, and so have no effect and are instantiated only for computational purposes.

We use a Bernoulli prior of weight q^n to make sure that each load b^n takes only values 0 or 1. Moreover, on each weight q^n, we place a conjugate Beta hyperprior

$$b^n | q^n \sim \text{Bernoulli}\left(q^n\right) \tag{36}$$

$$q^n \sim \text{Beta}\left(A_q, B_q\right). \tag{37}$$

To guarantee that the resulting formulation avoids overfitting, we make the specific choices $A_q = \alpha_q/N$ and $B_q = \beta_q(N-1)/N$. Under these choices [1, 15, 71, 72], and in the limit that $N \to \infty$ (that is, when the assumed biomolecule population is large), this prior/hyperprior choice converges to a non-parametric Beta-Bernoulli process. Consequently, for $N \gg 1$, the posterior remains well defined and becomes independent of the chosen value of N. In other words, provided N is large enough, its impact on the results is insignificant; while its precise value has only computational implications (see below) .

Summary of model equations

Below we list the equations used in our framework.

$$D \sim \text{InvGamma}\left(\alpha_D, \beta_D\right) \tag{38}$$

$$\mu_{part} \sim \text{Gamma}\left(\alpha_{part}, \beta_{mart}\right) \tag{39}$$

$$q^n \sim \text{Beta}\left(\frac{\alpha_q}{N}, \beta_q \frac{N-1}{N}\right) \tag{40}$$

$$b^n | q^n \sim \text{Bernoulli}(q^n) \tag{41}$$

$$\begin{cases} x_1^n \sim \text{SymNormal}\left(\mu_{xy}, \sigma_{xy}^2\right) \\ y_1^n \sim \text{SymNormal}\left(\mu_{xy}, \sigma_{xy}^2\right) \\ z_1^n \sim \text{SymNormal}\left(\mu_z, \sigma_z^2\right) \end{cases} \tag{42}$$

$$\begin{cases} x_k^n | x_{k-1}^n, D \sim \text{Normal}\left(x_{k-1}^n, 2\Delta t_{k-1} D\right), & k = 2, \ldots, K \\ y_k^n | y_{k-1}^n, D \sim \text{Normal}\left(y_{k-1}^n, 2\Delta t_{k-1} D\right), & k = 2, \ldots, K \\ z_k^n | z_{k-1}^n, D \sim \text{Normal}\left(z_{k-1}^n, 2\Delta t_{k-1} D\right), & k = 2, \ldots, K \end{cases} \tag{43}$$

$$\Delta t_{k-1} | \{x_k^n, y_k^n, z_k^n, b^n\}_n, \mu_{part} \sim \text{Exponential}\left(\mu_k \Delta t_{k-1}\right), \qquad k = 2, \ldots, K \tag{44}$$

$$\mu_k = \mu_{back} + \mu_{part} \sum_{n=1}^{N} b^n \exp\left(-2\frac{(x_k^n)^2 + (y_k^n)^2}{\omega_{xy}^2} - 2\frac{(z_k^n)^2}{\omega_z^2}\right) \tag{45}$$

Description of the computations

Here, $P(D, \mu_{part}, \{q^n, b^n, \overline{x}^n, \overline{y}^n, \overline{z}^n\}_n | \boldsymbol{\Delta t})$ is the joint probability distribution of our framework where biomolecular trajectories and measurements are gathered in

$$\overline{x}^n = (x_1^n, x_2^n, \ldots, x_K^n) \tag{46}$$

$$\overline{y}^n = (y_1^n, y_2^n, \ldots, y_K^n) \tag{47}$$

$$\overline{z}^n = (z_1^n, z_2^n, \ldots, z_K^n) \tag{48}$$

$$\boldsymbol{\Delta t} = (\Delta t_1, \Delta t_2, \ldots, \Delta t_{K-1}). \tag{49}$$

Posterior samples are generated according to Gibbs sampling [34, 61, 80, 92, 98] by updating each one of the involved variables sequentially. We achieve this by sampling a variable conditioned on all other variables and the given photon inter-arrival times $\boldsymbol{\Delta t}$. Conceptually, the steps involved in the generation of each posterior sample $(D, \mu_{part}, \{q^n, b^n, \overline{x}^n, \overline{y}^n, \overline{z}^n\}_n)$ are described below.

Since the locations of the inactive biomolecules do not contribute in the photon inter-arrival times $\boldsymbol{\Delta t}$, see Fig. (6) main text, and those locations are updated independently of the locations of the active ones, to make the algorithm computationally more efficient, we carry

out our sampling scheme in the following order:

1. For each n of the *active* biomolecules
   (a) Update trajectory $\overline{x}^n$ of active biomolecule n
   (b) Update trajectory $\overline{y}^n$ of active biomolecule n
   (c) Update trajectory $\overline{z}^n$ of active biomolecule n
2. Update jointly the trajectories $\overline{x}^n, \overline{y}^n, \overline{z}^n$ for all n of the *inactive* biomolecules
3. Update the diffusion coefficient D
4. Update jointly the prior weights q^n for all model biomolecules and simultaneously update jointly the loads b^n for all model biomolecules
5. Update the particle photon emission rate μ_{part}

These steps are described in detail below.

Sampling active biomolecules locations

To sample the location of an active biomolecule n in 3D, $(\overline{x}^n, \overline{y}^n, \overline{z}^n)$, we use forward filtering and backward sampling (FFBS) [9, 19, 50, 86]. In particular, we update each dimension sequentially from the following full conditional probability distributions $P(\overline{x}^n|D, \mu_{part}, \{b^{n'}, \overline{y}^{n'}, \overline{z}^{n'}\}_{n'}, \{\overline{x}^{n'}\}_{n'\neq n}, \boldsymbol{\Delta t})$, $P(\overline{y}^n|D, \mu_{part}, \{b^{n'}, \overline{x}^{n'}, \overline{z}^{n'}\}_{n'}, \{\overline{y}^{n'}\}_{n'\neq n}, \boldsymbol{\Delta t})$, and $P(\overline{z}^n|D, \mu_{part}, \{b^{n'}, \overline{x}^{n'}, \overline{y}^{n'}\}_{n'}, \{\overline{z}^{n'}\}_{n'\neq n}, \boldsymbol{\Delta t})$ for x, y, and z coordinates, respectively. Bellow, we show in detail the calculation only for sampling $\overline{x}^n$, since for sampling $\overline{y}^n$ and $\overline{z}^n$ they are similar.

Overview To sample the trajectory $\overline{x}^n$, we rely on the factorization

$$\begin{aligned}
&P(\overline{x}^n|D, \mu_{part}, \{b^{n'}, \overline{y}^{n'}, \overline{z}^{n'}\}_{n'}, \{\overline{x}^{n'}\}_{n'\neq n}, \boldsymbol{\Delta t}) \\
&= P(x^n_K|D, \mu_{part}, \{b^{n'}, \overline{y}^{n'}, \overline{z}^{n'}\}_{n'}, \{\overline{x}^{n'}\}_{n'\neq n}, \boldsymbol{\Delta t}) \\
&\times P(x^n_{K-1}|x^n_K, D, \mu_{part}, \{b^{n'}, \overline{y}^{n'}, \overline{z}^{n'}\}_{n'}, \{\overline{x}^{n'}\}_{n'\neq n}, \boldsymbol{\Delta t}) \\
&\times \cdots \qquad (50) \\
&\times P(x^n_2|x^n_1, D, \mu_{part}, \{b^{n'}, \overline{y}^{n'}, \overline{z}^{n'}\}_{n'}, \{\overline{x}^{n'}\}_{n'\neq n}, \boldsymbol{\Delta t}) \\
&\times P(x^n_1|D, \mu_{part}, \{b^{n'}, \overline{y}^{n'}, \overline{z}^{n'}\}_{n'}, \{\overline{x}^{n'}\}_{n'\neq n}, \boldsymbol{\Delta t})
\end{aligned}$$

and, according to this factorization, we sample individual locations x^n_k sequentially

$$x^n_K \sim P(x^n_K|D, \mu_{part}, \{b^{n'}, \overline{y}^{n'}, \overline{z}^{n'}\}_{n'}, \{\overline{x}^{n'}\}_{n'\neq n}, \boldsymbol{\Delta t}) \qquad (51)$$

$$x^n_k \sim P(x^n_k|x^n_{k+1}, D, \mu_{part}, \{b^{n'}, \overline{y}^{n'}, \overline{z}^{n'}\}_{n'}, \{\overline{x}^{n'}\}_{n'\neq n}, \boldsymbol{\Delta t}), \qquad (52)$$

Where, $k = 1, \ldots, K-1$. However, to be able to perform these steps, we first need to compute the involved probability distributions $P(x^n_k|x^n_{k+1}, D, \mu_{part}, \{b^{n'}, \overline{y}^{n'}, \overline{z}^{n'}\}_{n'}, \{\overline{x}^{n'}\}_{n'\neq n}, \boldsymbol{\Delta t})$. Below we describe a computationally efficient way to so that proceeds in a forward filtering and a backward sampling step that we present in detail.

Forward Filtering Before we start the sampling of the locations, we need to determine each one of the individual probability distributions that are needed in Eq. (52), $P(x^n_k|x^n_{k+1}, D, \mu_{part}, \{b^{n'}, \overline{y}^{n'}, \overline{z}^{n'}\}_{n'}, \{\overline{x}^{n'}\}_{n'\neq n}, \boldsymbol{\Delta t})$. To do this in a computationally tractable manner [13, 19], we compute filter distributions $P(x^n_k|D, \mu_{part}, \{b^{n'}, \overline{y}^{n'}, \overline{z}^{n'}\}_{n'}, \{\overline{x}^{n'}\}_{n'\neq n}, \{\Delta t_{k'}\}_{k'<k})$.

In our case, both dynamic (Eq. (43)) and observation (Eq. (44)) probability distributions provide equal probabilities for $+x^n_k$ and $-x^n_k$. Therefore, the filter distribution consists of two modes symmetrically placed across the origin [50]. Accordingly, we compute an *approximate* bimodal symmetric filter of the form

$$P\left(x^n_k|D, \mu_{part}, \{b^{n'}, \overline{y}^{n'}, \overline{z}^{n'}\}_{n'}, \{\overline{x}^{n'}\}_{n'\neq n}, \{\Delta t_{k'}\}_{k'<k}\right)$$

$$\approx \text{SymNormal}\left(x^n_k; m^n_k, c^n_k\right) \qquad (53)$$

where $\text{SymNormal}\left(m^n_k, c^n_k\right)$ describes the symmetric normal distribution (see Table II). The filter, that is the values of m^n_k and c^n_k, is updated iteratively according to

$$\begin{aligned}
&P\left(x^n_k|D, \mu_{part}, \{b^{n'}, \overline{y}^{n'}, \overline{z}^{n'}\}_{n'}, \{\overline{x}^{n'}\}_{n'\neq n}, \{\Delta t_{k'}\}_{k'<k}\right) \propto \\
&P\left(\Delta t_{k-1}|x^n_k, y^n_k, z^n_k, \mu_{part}, \{b^{n'}, x^{n'}, y^{n'}, z^{n'}\}'_n\right) \times \\
&\int_{x^n_{k-1}} P\left(x^n_{k-1}|D, \mu_{part}, \{b^{n'}, \overline{y}^{n'}, \overline{z}^{n'}\}_{n'}, \{\overline{x}^{n'}\}_{n'\neq n}, \{\Delta t_{k'}\}_{k'<k-1}\right) P\left(x^n_k|x^n_{k-1}, D\right) dx^n_{k-1}.
\end{aligned} \qquad (54)$$

To be able to carry out these computations efficiently, similar to [50], we work on an approximate model where the exponential emission equation, Eq. (44), is replaced by a normal one using the Wilson-Hiferty approximation as we discussed in section IV. Our *approximate* emission equation is

$$T_{data}\left(\Delta t_k\right)|\{x_k^n, y_k^n, z_k^n, b^n\}_n, \mu_{part}$$

$$\sim \text{Normal}\left(T_{mean}(\mu_k), S(\mu_k)^2\right), \quad k = 1, \ldots, K-1. \tag{55}$$

where μ_k is given in Eq. (45); while $T_{data}\left(\Delta t_k\right)$, $T_{mean}(\mu_k)$ and $S^2(\mu_k)$ are given by the Wilson-Hiferty approximation [101]. As explained in section IV, the approximation is given by

$$T_{data}(\Delta t_k) = \Delta t_k^{\frac{1}{3}}, \qquad T_{mean}(\mu_k) = \frac{8}{9\mu_k^{\frac{1}{3}}}, \qquad S^2(\mu_k) = \frac{1}{9\mu_k^{\frac{2}{3}}}. \tag{56}$$

Now, because of the specific choices of our problem (i.e. diffusive biomolecules, symmetric normal filter at the proceeding time, and normal likelihood), Eq. (54) reduces to

$$\begin{aligned} &P\left(x_k^n | D, \mu_{part}, \{b^{n'}, \overline{y}^{n'}, \overline{z}^{n'}\}_{n'}, \{\overline{x}^{n'}\}_{n' \neq n}, \{\Delta t_{k'}\}_{k'<k}\right) \\ &\quad = \text{Normal}\left(T_{data}(\Delta t_k); T_{mean}(\mu_k), S(\mu_k)^2\right) \times \\ &\quad \text{SymNormal}\left(x_k^n; m_{k-1}^n, c_{k-1}^n + 2D\Delta t_k\right) \end{aligned} . \tag{57}$$

Finally, to obtain the values of m_k^n and c_k^n, we linearize the product in Eq. (57) as described below.

From Eq. (57), we have

$$\text{Normal}\left(T_{data}(\Delta t_k); T_{mean}(\mu_k), S(\mu_k)^2\right) \times \tag{58}$$

$$\text{SymNormal}\left(x_k^n; m_{k-1}^n, c_{k-1}^n + 2D\Delta t_k\right) \tag{59}$$

$$= \text{Normal}\left(\sqrt[3]{\Delta t_{k-1}}; \frac{8}{9\sqrt[3]{\mu(x_k^n)}}, (\frac{1}{3\sqrt[3]{\mu(x_k^n)}})^2\right) \tag{60}$$

$$\times \left[\frac{1}{2}\text{Normal}(x_k^n; m_{k-1}^n, c_{k-1}^n + 2D\Delta t_{k-1})\right] + \tag{61}$$

$$\left[\frac{1}{2}\text{Normal}(x_k^n; -m_{k-1}^n, c_{k-1}^n + 2D\Delta t_{k-1})\right] \tag{62}$$

$$\begin{aligned} &\propto \exp\left(\frac{\log\mu(x_k^n)}{3} - \frac{\left(\frac{8}{9} - \sqrt[3]{\mu(x_k^n)\Delta t_{k-1}}\right)^2}{\frac{2}{9}} - \frac{(x_k^n - m_{k-1}^n)^2}{2(c_{k-1}^n + 2D\Delta t_{k-1})}\right) \\ &+ \exp\left(\frac{\log\mu(x_k^n)}{3} - \frac{\left(\frac{8}{9} - \sqrt[3]{\mu(x_k^n)\Delta t_{k-1}}\right)^2}{\frac{2}{9}} - \frac{(x_k^n + m_{k-1}^n)^2}{2(c_{k-1}^n + 2D\Delta t_{k-1})}\right). \end{aligned} \tag{63}$$

The density in Eq. (63) consists of two modes, one on the positive semi-axis of x and one on the negative semi-axis of x. Considering $f(x_k^n) = \sqrt[3]{\mu(x_k^n)\Delta t_{k-1}}$ and $g(x_k^n) = \frac{1}{3}\log\mu(x_k^n)$ and linearizing them around the previous filter's mode, $+m_{k-1}^n$, the fist mode of Eq. (63) is approximated by

$$\begin{aligned} &\exp\left(\frac{\log\mu(x_k^n)}{3} - \frac{\left(\frac{8}{9} - \sqrt[3]{\mu(x_k^n)\Delta t_{k-1}}\right)^2}{\frac{2}{9}} - \frac{(x_k^n - m_{k-1}^n)^2}{2(c_{k-1}^n + 2D\Delta t_{k-1})}\right) \\ &\approx \exp\left(v_1 x_k^n - \frac{(x_k^n - h_1)^2}{\frac{2\sigma^2}{f'(-m_{k-1}^n)^2}} - \frac{(x_k^n - m_{k-1}^n)^2}{2(c_{k-1}^n + 2D\Delta t_{k-1})}\right). \end{aligned} \tag{64}$$

Similarly, linearizing $f(x_k^n)$ and $g(x_k^n)$ around $-m_{k-1}^n$, the second mode of Eq. (63) is approximated by

$$\exp\left(\frac{\log\mu(x_k^n)}{3} - \frac{\left(\frac{8}{9} - \sqrt[3]{\mu(x_k^n)\Delta t_{k-1}}\right)^2}{\frac{2}{9}} - \frac{(x_k^n + m_{k-1}^n)^2}{2(c_{k-1}^n + 2D\Delta t_{k-1})}\right)$$
$$\approx \exp\left(v_2 x_k^n - \frac{(x_k^n - h_2)^2}{\frac{2\sigma^2}{f'(-m_{k-1}^n)^2}} - \frac{(x_k^n + m_{k-1}^n)^2}{2(c_{k-1}^n + 2D\Delta t_{k-1})}\right). \tag{65}$$

Combining both mode approximations, the density of Eq. (63), is approximated by

$$\exp\left(\frac{\log\mu(x_k^n)}{3} - \frac{\left(\frac{8}{9} - \sqrt[3]{\mu(x_k^n)\Delta t_{k-1}}\right)^2}{\frac{2}{9}} - \frac{(x_k^n - m_{k-1}^n)^2}{2(c_{k-1}^n + 2D\Delta t_{k-1})}\right)$$
$$+ \exp\left(\frac{\log\mu(x_k^n)}{3} - \frac{\left(\frac{8}{9} - \sqrt[3]{\mu(x_k^n)\Delta t_{k-1}}\right)^2}{\frac{2}{9}} - \frac{(x_k^n + m_{k-1}^n)^2}{2(c_{k-1}^n + 2D\Delta t_{k-1})}\right)$$
$$\approx \exp\left(v_1 x_k^n - \frac{(x_k^n - h_1)^2}{\frac{2\sigma^2}{f'(+m_{k-1}^n)^2}} - \frac{(x_k^n - m_{k-1}^n)^2}{2(\mathbf{c}_{i,n-1}^k + 2D\Delta t_{k-1})}\right)$$
$$+ \exp\left(v_2 x_k^n - \frac{(x_k^n - h_2)^2}{\frac{2\sigma^2}{f'(-m_{k-1}^n)^2}} - \frac{(x_k^n + m_{k-1}^n)^2}{2(c_{k-1}^n + 2D\Delta t_{k-1})}\right) \tag{66}$$

where we use the following definitions

$$h_1 = \frac{\frac{8}{9} - f(+m_{k-1}^n) + m_{k-1}^n f'(+m_{k-1}^n)}{f'(+m_{k-1}^n)}$$
$$v_1 = \frac{\mu'(+m_{k-1}^n)}{3\mu(+m_{k-1}^n)} \tag{67}$$

$$h_2 = \frac{\frac{8}{9} - f(-m_{k-1}^n) - m_{k-1}^n f'(-m_{k-1}^n)}{f'(-m_{k-1}^n)}$$
$$v_2 = \frac{\mu'(-m_{k-1}^n)}{3\mu(-m_{k-1}^n)}. \tag{68}$$

The formula in Eq. (66) describes a probability density of a symmetric normal distribution. Equating this distribution with our filter, i.e., SymNormal (m_k^n, c_k^n), we obtain

$$c_k^n = \frac{1}{\frac{1}{c_{k-1}^n + 2D\Delta t_{k-1}} + \frac{9}{2} f'(m_{k-1}^n)^2} \tag{69}$$
$$m_k^n = \left(v_1 + 9h_1 f'(m_{k-1}^n)^2 + \frac{m_{k-1}^n}{c_{k-1}^n + 2D\Delta t_{k-1}}\right) c_k^n. \tag{70}$$

These equations apply for $k = 2, \ldots, K$ and can be used to update the filter. To begin, we use Eq. (42) and set $c_1^n = \sigma_{xy}^2$ and $m_1^n = \mu_{xy}$.

Backward sampling Having computed the filter distributions above, we are able to sample the individual locations according to Eq. (51) and Eq. (52) by starting from x_K^n and moving backward towards x_1^n. In particular, by applying the Bayes' rule, each one of the individual distributions on Eq. (52) factorize as

$$P(x_k^n | x_{k+1}^n, D, \mu_{part}, \{b^{n'}, \overline{y}^{n'}, \overline{z}^{n'}\}_{n'}, \{\overline{x}^{n'}\}_{n' \neq n}, \mathbf{\Delta t}) \propto$$
$$P\left(x_k^n | D, \mu_{part}, \{b^{n'}, \overline{y}^{n'}, \overline{z}^{n'}\}_{n'}, \{\overline{x}^{n'}\}_{n' \neq n}, \{\Delta t_{k'}\}_{k' < k}\right) \times P\left(x_k^n | x_{k+1}^n, D\right). \tag{71}$$

In the above, the first term is given by the filter distribution which is replaced by our approximate

SymNormal(m_k^n, c_k^n), and the second term is our motion model Normal$(x_k^n, 2D\Delta t_{k-1})$, all of which are known at this stage. Therefore, the sampling distributions become

$$x_K^n \sim \frac{1}{2}\text{Normal}\left(+m_K^n, c_K^n\right) + \frac{1}{2}\text{Normal}\left(-m_K^n, c_K^n\right) \tag{72}$$

$$\begin{aligned} x_{k-1}^n \sim & \frac{\exp\left[\frac{(x_k^n - m_k^n)^2}{c_k^n + 2D\Delta t_{k-1}}\right]}{2\sqrt{2\pi(c_k^n + 2D\Delta t_{k-1})}}\text{Normal}\left(\frac{x_k^n c_k^n + 2D\Delta t_{k-1} m_k^n}{c_k^n + 2D\Delta t_{k-1}}, \frac{2D\Delta t_{k-1} c_k^n}{c_k^n + 2D\Delta t_{k-1}}\right) \\ & + \frac{\exp\left[\frac{(x_k^n + m_k^n)^2}{c_k^n + 2D\Delta t_{k-1}}\right]}{2\sqrt{2\pi(c_k^n + 2D\Delta t_{k-1})}}\text{Normal}\left(\frac{x_k^n c_k^n - 2D\Delta t_{k-1} m_k^n}{c_k^n + 2D\Delta t_{k-1}}, \frac{2D\Delta t_{k-1} c_k^n}{c_k^n + 2D\Delta t_{k-1}}\right) \\ & , \quad k = 2, \ldots, K. \end{aligned} \tag{73}$$

Sampling inactive biomolecule trajectories

When we update the trajectories of the active biomolecules, the next step is the update of the trajectories of the inactive ones. To do this, we sample from the corresponding conditionals $P(\overline{x}^n, \overline{y}^n, \overline{z}^n | D, \mu_{part}, \{q^n, b^n\}_n, \boldsymbol{\Delta t})$. Since the locations of inactive biomolecules are not associated with the observations in $\boldsymbol{\Delta t}$, these conditionals simplify to $P(\overline{x}^n, \overline{y}^n, \overline{z}^n | D, \{q^n, b^n\}_n)$ which can be readily simulated jointly in the same manner as standard 3D Brownian motion [59].

Sampling the diffusion coefficient

We sample the diffusion coefficient from the conditional probability distribution $P(D|\mu_{part}, \{q^n, b^n, \overline{x}^n, \overline{y}^n, \overline{z}^n\}_n, \boldsymbol{\Delta t})$. Because of the specific dependencies of the variables in this formulation, e.g. Eq. (31) and Eq. (43), the conditional distribution simplifies to $P(D|\{\overline{x}^n, \overline{y}^n, \overline{z}^n\}_n, \boldsymbol{\Delta t})$. Using Bays' rule, this distribution becomes

$$D \sim \text{InvGamma}(\alpha'_D, \beta'_D) \tag{74}$$

where the parameters α'_D and β'_D are given by

$$\alpha'_D = \alpha_D + \frac{3N(K-1)}{2} \tag{75}$$

$$\beta'_D = \beta_D + \frac{1}{4}\sum_{k=2}^{K} \frac{\sum_{n=1}^{N}\left(\left(x_k^n - x_{k-1}^n\right)^2 + \left(y_k^n - y_{k-1}^n\right)^2 + \left(z_k^n - z_{k-1}^n\right)^2\right)}{\Delta t_{k-1}}. \tag{76}$$

Sampling biomolecule loads

For each biomolecule n we sample its load prior weight, q^n, from the corresponding conditional distribution $P(q^n|\mu_{part}, D, \{b^n, \overline{x}^n, \overline{y}^n, \overline{z}^n\}_n, \boldsymbol{\Delta t})$, which simplifies to $P(q^n|b^n)$. To do this we use Eq. (41) and Eq. (40). According to Bays' rule, the latter distribution becomes

$$q^n \sim \text{Beta}(\alpha', \beta') \tag{77}$$

where $\alpha' = \frac{\alpha}{N} + b^n$ and $\beta' = \beta\frac{N-1}{N} + 1 - b^n$.

Once the weights q^n or all biomolecules are updated from the above procedure, we update the loads b^n by sampling from the corresponding conditional distribution $P(\{b^n\}_n|D, \mu_{part}, \{q^n, \overline{x}^n, \overline{y}^n, \overline{z}^n\}_n, \boldsymbol{\Delta t})$ using a Methropolis-Hasting algorithm [17, 21]. For this, we use a proposal distribution with the form

$$b_{new}^n \sim \text{Bernoulli}(q^n). \tag{78}$$

With this proposal, the acceptance ratio becomes

$$r = \prod_{k=1}^{K-1} \frac{\left[\mu_{back} + \mu_{part} \sum_{n=1}^{N} b^n_{new} \exp\left(-2\frac{(x^n_k)^2+(y^n_k)^2}{\omega^2_{xy}} - 2\frac{(z^n_k)^2}{\omega^2_z}\right)\right]}{\left[\mu_{back} + \mu_{part} \sum_{n=1}^{N} b^n_{old} \exp\left(-2\frac{(x^n_k)^2+(y^n_k)^2}{\omega^2_{xy}} - 2\frac{(z^n_k)^2}{\omega^2_z}\right)\right]} \times \prod_{k=1}^{K-1} \frac{e^{-\left[\mu_{back}+\mu_{part}\sum_{n=1}^{N} b^n_{new} \exp\left(-2\frac{(x^n_k)^2+(y^n_k)^2}{\omega^2_{xy}} - 2\frac{(z^n_k)^2}{\omega^2_z}\right)\right]\Delta t_k}}{e^{-\left[\mu_{back}+\mu_{part}\sum_{n=1}^{N} b^n_{old} \exp\left(-2\frac{(x^n_k)^2+(y^n_k)^2}{\omega^2_{xy}} - 2\frac{(z^n_k)^2}{\omega^2_z}\right)\right]\Delta t_k}}. \tag{79}$$

Sampling the particle photon emission rate

In the last step, after updating the locations and loads of the biomolecules, we sample the particle photon emission rate from the corresponding conditional distribution $P(\mu_{part}|D, \{q^n, b^n, \overline{x}^n, \overline{y}^n, \overline{z}^n\}_n, \boldsymbol{\Delta t})$. To sample this distribution, we also use a Metropolis-Hastings step. For this, we use proposals of the form

$$\mu^{new}_{part} \sim \text{Gamma}\left(\alpha_{part}, \frac{\mu^{old}_{part}}{\alpha_{part}}\right) \tag{80}$$

where μ^{old}_{part} denotes the current sampled value. Using both Eqs. (44) and (45), the acceptance ratio becomes

$$\begin{aligned} r = \exp &\left[\sum_{k=1}^{K-1} \log\left(\frac{\mu_{back} + \mu^{new}_{part} \sum_{n=1}^{N} b^n \exp\left(-2\frac{(x^n_k)^2+(y^n_k)^2}{\omega^2_{xy}} - 2\frac{(z^n_k)^2}{\omega^2_z}\right)}{\mu_{back} + \mu^{old}_{part} \sum_{n=1}^{N} b^n \exp\left(-2\frac{(x^n_k)^2+(y^n_k)^2}{\omega^2_{xy}} - 2\frac{(z^n_k)^2}{\omega^2_z}\right)}\right)\right] \\ &\times \exp\left[\sum_{k=1}^{K-1}\left[(\mu^{old}_{part} - \mu^{new}_{part})\Delta t_k \sum_{n=1}^{N} b^n \exp\left(-2\frac{(x^n_k)^2+(y^n_k)^2}{\omega^2_{xy}} - 2\frac{(z^n_k)^2}{\omega^2_z}\right)\right]\right] \\ &\times \exp\left[(\alpha_{part}-1)\log\left(\frac{\mu^{new}_{part}}{\mu^{old}_{part}}\right) + \frac{1}{\beta_{part}}(\mu^{old}_{part} - \mu^{new}_{part}) + (2\alpha - 1)\log\left(\frac{\mu^{old}_{part}}{\mu^{new}_{part}}\right)\right] \\ &\times \exp\left[\alpha\left(\frac{\mu^{new}_{part}}{\mu^{old}_{part}} - \frac{\mu^{old}_{part}}{\mu^{new}_{part}}\right)\right]. \end{aligned} \tag{81}$$

In the above ratio, α_{part} and β_{part} are parameters of the prior and α is the parameter of the proposal.

[1] Luai Al Labadi and Mahmoud Zarepour. On approximations of the beta process in latent feature models: Point processes approach. *Sankhya A*, 80(1):59–79, 2018.

[2] Michael Andrec, Ronald M Levy, and David S Talaga. Direct determination of kinetic rates from single-molecule photon arrival trajectories using hidden markov models. *The Journal of Physical Chemistry A*, 107(38):7454–7464, 2003.

[3] JO Andrews, W Conway, W-K Cho, A Narayanan, J-H Spille, N Jayanth, T Inoue, S Mullen, J Thaler, and II Cissé. qSR: A quantitative super-resolution analysis tool reveals the cell-cycle dependent organization of RNA polymerase i in live human cells. *Scientific Reports*, 8(1):7424, 2018.

[4] Daniel Axelrod, DE Koppel, J Schlessinger, Ei Elson, and Watt W Webb. Mobility measurement by analysis of fluorescence photobleaching recovery kinetics. *Biophysical Journal*, 16(9):1055–1069, 1976.

[5] A Benda, M Beneš, V Marecek, A Lhotskỳ, W Th Hermens, and M Hof. How to determine diffusion coefficients in planar phospholipid systems by confocal fluorescence correlation spectroscopy. *Langmuir*, 19(10): 4120–4126, 2003.

[6] Howard C Berg. *Random walks in biology*. Princeton University Press, 1993.

[7] Andrew J Berglund. Statistics of camera-based single-particle tracking. *Physical Review E*, 82(1):011917, 2010.

[8] Robert B Best and Gerhard Hummer. Reaction coordinates and rates from transition paths. *Proceedings of the National Academy of Sciences*, 102(19):6732–6737, 2005.

[9] Christopher M Bishop. *Pattern recognition and machine learning*. springer, 2006.

[10] Hans Blom and Gunnar Björk. Lorentzian spatial intensity distribution in one-photon fluorescence correlation spectroscopy. *Applied Optics*, 48(31):6050–6058, 2009.

[11] Max Born and Emil Wolf. *Principles of optics: electromagnetic theory of propagation, interference and diffraction of light*. Elsevier, 2013.

[12] GJ Brakenhoff, K Visscher, and HTM Van der Voort. Size and shape of the confocal spot: control and relation to 3D imaging and image processing. In *Handbook of biological confocal microscopy*, pages 87–91. Springer, 1990.

[13] Mark Briers, Arnaud Doucet, and Simon Maskell. Smoothing algorithms for state–space models. *Annals of the Institute of Statistical Mathematics*, 62(1):61, 2010.

[14] Gary R Bright, Gregory W Fisher, Jadwiga Rogowska, and D Lansing Taylor. Fluorescence ratio imaging microscopy. *Methods in Cell Biology*, 30:157–192, 1989.

[15] Tamara Broderick, Michael I Jordan, Jim Pitman, et al. Beta processes, stick-breaking and power laws. *Bayesian Analysis*, 7(2):439–476, 2012.

[16] Jonathan E Bronson, Jingyi Fei, Jake M Hofman, Ruben L Gonzalez Jr, and Chris H Wiggins. Learning rates and states from biophysical time series: a bayesian approach to model selection and single-molecule FRET data. *Biophysical Journal*, 97(12):3196–3205, 2009.

[17] Ben Calderhead. A general construction for parallelizing metropolis- hastings algorithms. *Proceedings of the National Academy of Sciences*, 111(49):17408–17413, 2014.

[18] Christopher P Calderon and Kerry Bloom. Inferring latent states and refining force estimates via hierarchical dirichlet process modeling in single particle tracking experiments. *PloS one*, 10(9):e0137633, 2015.

[19] Olivier Cappé, Eric Moulines, and Tobias Rydén. Inference in hidden markov models. In *Proceedings of EUSFLAT Conference*, pages 14–16, 2009.

[20] Yan Chen, Joachim D Müller, Peter TC So, and Enrico Gratton. The photon counting histogram in fluorescence fluctuation spectroscopy. *Biophysical Journal*, 77(1):553–567, 1999.

[21] Siddhartha Chib and Edward Greenberg. Understanding the metropolis-hastings algorithm. *The american statistician*, 49(4):327–335, 1995.

[22] Daniel T Chiu, Noo Li Jeon, Sui Huang, Ravi S Kane, Christopher J Wargo, Insung S Choi, Donald E Ingber, and George M Whitesides. Patterned deposition of cells and proteins onto surfaces by using three-dimensional microfluidic systems. *Proceedings of the National Academy of Sciences*, 97(6):2408–2413, 2000.

[23] Hoi Sung Chung and Irina V Gopich. Fast single-molecule FRET spectroscopy: theory and experiment. *Physical Chemistry Chemical Physics*, 16(35):18644–18657, 2014.

[24] Hoi Sung Chung, Fanjie Meng, Jae-Yeol Kim, Kevin McHale, Irina V Gopich, and John M Louis. Oligomerization of the tetramerization domain of p53 probed by two-and three-color single-molecule FRET. *Proceedings of the National Academy of Sciences*, page 201700357, 2017.

[25] Petra Dittrich, Flaminia Malvezzi-Campeggi, Michael Jahnz, and Petra Schwille. Accessing molecular dynamics in cells by fluorescence correlation spectroscopy. *Biological chemistry*, 382(3):491–494, 2001.

[26] Elliot L Elson. Fluorescence correlation spectroscopy: past, present, future. *Biophysical journal*, 101(12):2855–2870, 2011.

[27] Elliot L Elson and Douglas Magde. Fluorescence correlation spectroscopy. I. conceptual basis and theory. *Biopolymers*, 13(1):1–27, 1974.

[28] Jörg Enderlein and W Patrick Ambrose. Optical collection efficiency function in single-molecule detection experiments. *Applied optics*, 36(22):5298–5302, 1997.

[29] Jorg Enderlein, Ingo Gregor, Digambara Patra, and Jorg Fitter. Art and artefacts of fluorescence correlation spectroscopy. *Current pharmaceutical biotechnology*, 5 (2):155–161, 2004.

[30] Radek Erban and S Jonathan Chapman. Stochastic modelling of reaction–diffusion processes: algorithms for bimolecular reactions. *Physical Biology*, 6(4):046001, 2009.

[31] Thomas S Ferguson. A Bayesian analysis of some nonparametric problems. *The Annals of Statistics*, pages 209–230, 1973.

[32] James AJ Fitzpatrick and Björn F Lillemeier. Fluorescence correlation spectroscopy: linking molecular dynamics to biological function in vitro and in situ. *Current Opinion in Structural Biology*, 21(5):650–660, 2011.

[33] Andreas Gahlmann and WE Moerner. Exploring bacterial cell biology with single-molecule tracking and super-resolution imaging. *Nature Reviews Microbiology*, 12(1): 9, 2014.

[34] Andrew Gelman, John B Carlin, Hal S Stern, David B Dunson, Aki Vehtari, and Donald B Rubin. *Bayesian data analysis*, volume 2. CRC press Boca Raton, FL, 2014.

[35] P-O Gendron, F Avaltroni, and KJ Wilkinson. Diffusion coefficients of several rhodamine derivatives as determined by pulsed field gradient–nuclear magnetic resonance and fluorescence correlation spectroscopy. *Journal of Fluorescence*, 18(6):1093, 2008.

[36] Sarah Frisken Gibson and Frederick Lanni. Experimental test of an analytical model of aberration in an oil-immersion objective lens used in three-dimensional light microscopy. *JOSA A*, 9(1):154–166, 1992.

[37] Irina V Gopich. Accuracy of maximum likelihood estimates of a two-state model in single-molecule FRET. *The Journal of Chemical Physics*, 142(3):034110, 2015.

[38] Irina V Gopich and Attila Szabo. Single-molecule FRET with diffusion and conformational dynamics. *The Journal of Physical Chemistry B*, 111(44):12925–12932, 2007.

[39] Irina V Gopich and Attila Szabo. Decoding the pattern of photon colors in single-molecule FRET. *The Journal of Physical Chemistry B*, 113(31):10965–10973, 2009.

[40] Irina V Gopich and Attila Szabo. Theory of the energy transfer efficiency and fluorescence lifetime distribution in single-molecule FRET. *Proceedings of the National Academy of Sciences*, 109(20):7747–7752, 2012.

[41] Taekjip Ha, Alice Y Ting, Joy Liang, W Brett Caldwell, Ashok A Deniz, Daniel S Chemla, Peter G Schultz,

and Shimon Weiss. Single-molecule fluorescence spectroscopy of enzyme conformational dynamics and cleavage mechanism. *Proceedings of the National Academy of Sciences*, 96(3):893–898, 1999.

[42] JM Haile, Ian Johnston, A John Mallinckrodt, Susan McKay, et al. Molecular dynamics simulation: elementary methods. *Computers in Physics*, 7(6):625–625, 1993.

[43] Marta Hajdziona and Andrzej Molski. Maximum likelihood-based analysis of single-molecule photon arrival trajectories. *The Journal of Chemical Physics*, 134 (5):054112, 2011.

[44] Jun He, Syuan-Ming Guo, and Mark Bathe. Bayesian approach to the analysis of fluorescence correlation spectroscopy data i: theory. *Analytical Chemistry*, 84(9): 3871–3879, 2012.

[45] Desmond J Higham. An algorithmic introduction to numerical simulation of stochastic differential equations. *SIAM Review*, 43(3):525–546, 2001.

[46] Keegan E Hines. A primer on Bayesian inference for biophysical systems. *Biophysical Journal*, 108(9):2103–2113, 2015.

[47] Keegan E Hines, John R Bankston, and Richard W Aldrich. Analyzing single-molecule time series via nonparametric Bayesian inference. *Biophysical Journal*, 108 (3):540–556, 2015.

[48] Bo Huang, Mark Bates, and Xiaowei Zhuang. Superresolution fluorescence microscopy. *Annual Review of Biochemistry*, 78:993–1016, 2009.

[49] Oliver C Ibe. *Elements of Random Walk and Diffusion Processes*. John Wiley & Sons, 2013.

[50] Sina Jazani, Ioannis Sgouralis, and Steve Pressé. A method for single molecule tracking using a conventional single-focus confocal setup. *The Journal of Chemical Physics*, 2019 (to appear).

[51] Margaret E Johnson and Gerhard Hummer. Free-propagator reweighting integrator for single-particle dynamics in reaction-diffusion models of heterogeneous protein-protein interaction systems. *Physical Review X*, 4(3):031037, 2014.

[52] Oleg Krichevsky and Grégoire Bonnet. Fluorescence correlation spectroscopy: the technique and its applications. *Reports on Progress in Physics*, 65(2):251, 2002.

[53] Lucas Lacasa, Inés P Mariño, Joaquin Miguez, Vincenzo Nicosia, Édgar Roldán, Ana Lisica, Stephan W Grill, and Jesús Gómez-Gardeñes. Multiplex decomposition of non-markovian dynamics and the hidden layer reconstruction problem. *Physical Review X*, 8(3):031038, 2018.

[54] Joseph R Lakowicz. *Principles of fluorescence spectroscopy*. Springer, 2006.

[55] Antony Lee, Konstantinos Tsekouras, Christopher Calderon, Carlos Bustamante, and Steve Pressé. Unraveling the thousand word picture: An introduction to super-resolution data analysis. *Chemical Reviews*, 2017.

[56] Sang-Hyuk Lee, Jae Yen Shin, Antony Lee, and Carlos Bustamante. Counting single photoactivatable fluorescent molecules by photoactivated localization microscopy (palm). *Proceedings of the National Academy of Sciences*, 2012.

[57] Eitan Lerner, Antonino Ingargiola, and Shimon Weiss. Characterizing highly dynamic conformational states: the transcription bubble in rnap-promoter open complex as an example. *The Journal of Chemical Physics*, 148(12):123315, 2018.

[58] Hui Li, Chi-Fu Yen, and Sanjeevi Sivasankar. Fluorescence axial localization with nanometer accuracy and precision. *Nano Letters*, 12(7):3731–3735, 2012.

[59] Lawrence C-L Lin and Frank LH Brown. Brownian dynamics in fourier space: membrane simulations over long length and time scales. *Physical review letters*, 93 (25):256001, 2004.

[60] Hongchao Liu, Bo Jiu, Hongwei Liu, and Zheng Bao. Superresolution isar imaging based on sparse bayesian learning. *IEEE Transactions on Geoscience and Remote Sensing*, 52(8):5005–5013, 2014.

[61] Huan Liu and Hiroshi Motoda. *Computational methods of feature selection*. CRC Press, 2007.

[62] Zhe Liu, Luke D Lavis, and Eric Betzig. Imaging live-cell dynamics and structure at the single-molecule level. *Molecular cell*, 58(4):644–659, 2015.

[63] Radek Macháň and Martin Hof. Lipid diffusion in planar membranes investigated by fluorescence correlation spectroscopy. *Biochimica et Biophysica Acta (BBA)-Biomembranes*, 1798(7):1377–1391, 2010.

[64] Douglas Magde, Elliot L Elson, and Watt W Webb. Fluorescence correlation spectroscopy. II. an experimental realization. *Biopolymers*, 13(1):29–61, 1974.

[65] Valentin Magidson and Alexey Khodjakov. Circumventing photodamage in live-cell microscopy. In *Methods in cell biology*, volume 114, pages 545–560. Elsevier, 2013.

[66] Sean P Meyn and Richard L Tweedie. Stability of markovian processes ii: Continuous-time processes and sampled chains. *Advances in Applied Probability*, 25(3): 487–517, 1993.

[67] Sean P Meyn and Richard L Tweedie. Stability of markovian processes iii: Foster–lyapunov criteria for continuous-time processes. *Advances in Applied Probability*, 25(3):518–548, 1993.

[68] X Michalet, OHW Siegmund, JV Vallerga, P Jelinsky, JE Millaud, and S Weiss. Detectors for single-molecule fluorescence imaging and spectroscopy. *Journal of modern optics*, 54(2-3):239–281, 2007.

[69] Arjun Narayanan, Anatoli B Meriin, Michael Y Sherman, and Ibrahim I Cisse. A first order phase transition underlies the formation of sub-diffractive protein aggregates in mammalian cells. *bioRxiv*, page 148395, 2017.

[70] Kenji Okamoto and Yasushi Sako. Variational bayes analysis of a photon-based hidden markov model for single-molecule FRET trajectories. *Biophysical Journal*, 103(6):1315–1324, 2012.

[71] John Paisley and Lawrence Carin. Nonparametric factor analysis with beta process priors. In *Proceedings of the 26th Annual International Conference on Machine Learning*, pages 777–784. ACM, 2009.

[72] John Paisley and Michael I Jordan. A constructive definition of the beta process. *arXiv preprint arXiv:1604.00685*, 2016.

[73] Konstantina Palla, David A Knowles, and Zoubin Ghahramani. A reversible infinite HMM using normalised random measures. In *International Conference on Machine Learning*, 2014.

[74] Robert D Phair and Tom Misteli. Kinetic modelling approaches to in vivo imaging. *Nature Reviews Molecular Cell Biology*, 2(12):898, 2001.

[75] Rob Phillips, Julie Theriot, Jane Kondev, and Hernan

Garcia. *Physical biology of the cell*. Garland Science, 2012.

[76] Menahem Pirchi, Roman Tsukanov, Rashid Khamis, Toma E Tomov, Yaron Berger, Dinesh C Khara, Hadas Volkov, Gilad Haran, and Eyal Nir. Photon-by-photon hidden markov model analysis for microsecond single-molecule FRET kinetics. *The Journal of Physical Chemistry B*, 120(51):13065–13075, 2016.

[77] Martin Purschke, Noemi Rubio, Kathryn D Held, and Robert W Redmond. Phototoxicity of hoechst 33342 in time-lapse fluorescence microscopy. *Photochemical & Photobiological Sciences*, 9(12):1634–1639, 2010.

[78] Katrien Remaut, Bart Lucas, Kevin Braeckmans, NN Sanders, SC De Smedt, and Jo Demeester. FRET-FCS as a tool to evaluate the stability of oligonucleotide drugs after intracellular delivery. *Journal of Controlled Release*, 103(1):259–271, 2005.

[79] Rudolf Rigler and Elliot S Elson. *Fluorescence correlation spectroscopy: theory and applications*, volume 65. Springer Science & Business Media, 2012.

[80] Christian Robert and George Casella. *Introducing Monte Carlo Methods with R*. Springer Science & Business Media, 2009.

[81] Dag Scherfeld, Nicoletta Kahya, and Petra Schwille. Lipid dynamics and domain formation in model membranes composed of ternary mixtures of unsaturated and saturated phosphatidylcholines and cholesterol. *Biophysical Journal*, 85(6):3758–3768, 2003.

[82] Patrick D Schmidt, Benjamin H Reichert, John G Lajoie, and Sanjeevi Sivasankar. Method for high frequency tracking and sub-nm sample stabilization in single molecule fluorescence microscopy. *Scientific reports*, 8(1):13912, 2018.

[83] Petra Schwille and Elke Haustein. Fluorescence correlation spectroscopy: an introduction to its concepts and applications. *Biophysics textbook online*, 1(3), 2001.

[84] Petra Schwille, Franz-Josef Meyer-Almes, and Rudolf Rigler. Dual-color fluorescence cross-correlation spectroscopy for multicomponent diffusional analysis in solution. *Biophysical Journal*, 72(4):1878–1886, 1997.

[85] Petra Schwille, Ulrich Haupts, Sudipta Maiti, and Watt W Webb. Molecular dynamics in living cells observed by fluorescence correlation spectroscopy with one-and two-photon excitation. *Biophysical journal*, 77 (4):2251–2265, 1999.

[86] Steven L Scott. Bayesian methods for hidden markov models: Recursive computing in the 21st century. *Journal of the American Statistical Association*, 97(457): 337–351, 2002.

[87] Ioannis Sgouralis and Steve Pressé. Icon: an adaptation of infinite hmms for time traces with drift. *Biophysical Journal*, 112(10):2117–2126, 2017.

[88] Ioannis Sgouralis and Steve Pressé. An introduction to infinite HMMs for single-molecule data analysis. *Biophysical Journal*, 112(10):2021–2029, 2017.

[89] Ioannis Sgouralis, Shreya Madaan, Franky Djutanta, Rachael Kha, Rizal F Hariadi, and Steve Pressé. A bayesian nonparametric approach to single molecule forster resonance energy transfer. *The Journal of Physical Chemistry B*, 123(3):675–688, 2018.

[90] Ioannis Sgouralis, Miles Whitmore, Lisa Lapidus, Matthew J Comstock, and Steve Pressé. Single molecule force spectroscopy at high data acquisition: A bayesian nonparametric analysis. *The Journal of Chemical Physics*, 148(12):123320, 2018.

[91] Jesse Stricker, Paul Maddox, ED Salmon, and Harold P Erickson. Rapid assembly dynamics of the escherichia coli ftsz-ring demonstrated by fluorescence recovery after photobleaching. *Proceedings of the National Academy of Sciences*, 99(5):3171–3175, 2002.

[92] Meysam Tavakoli, J Nicholas Taylor, Chun-Biu Li, Tamiki Komatsuzaki, and Steve Pressé. Single molecule data analysis: an introduction. *arXiv preprint arXiv:1606.00403*, 2016.

[93] Yee W Teh, Michael I Jordan, Matthew J Beal, and David M Blei. Sharing clusters among related groups: Hierarchical dirichlet processes. In *Advances in neural information processing systems*, pages 1385–1392, 2005.

[94] Jean-Yves Tinevez, Joe Dragavon, Lamya Baba-Aissa, Pascal Roux, Emmanuelle Perret, Astrid Canivet, Vincent Galy, and Spencer Shorte. A quantitative method for measuring phototoxicity of a live cell imaging microscope. In *Methods in enzymology*, volume 506, pages 291–309. Elsevier, 2012.

[95] Tedman Torres and Marcia Levitus. Measuring conformational dynamics: a new FCS-FRET approach. *The Journal of Physical Chemistry B*, 111(25):7392–7400, 2007.

[96] Konstantinos Tsekouras, Amanda P Siegel, Richard N Day, and Steve Pressé. Inferring diffusion dynamics from FCS in heterogeneous nuclear environments. *Biophysical Journal*, 109(1):7–17, 2015.

[97] Stephan Uphoff, Kristofer Gryte, Geraint Evans, and Achillefs N Kapanidis. Improved temporal resolution and linked hidden markov modeling for switchable single-molecule FRET. *ChemPhysChem*, 12(3):571–579, 2011.

[98] Udo Von Toussaint. Bayesian inference in physics. *Reviews of Modern Physics*, 83(3):943, 2011.

[99] Marta Waligórska and Andrzej Molski. Maximum likelihood-based analysis of photon arrival trajectories in single-molecule fret. *Chemical Physics*, 403:52–58, 2012.

[100] Shimon Weiss. Fluorescence spectroscopy of single biomolecules. *Science*, 283(5408):1676–1683, 1999.

[101] Edwin B Wilson and Margaret M Hilferty. The distribution of chi-square. *Proceedings of the National Academy of Sciences*, 17(12):684–688, 1931.

[102] Thorsten Wohland, Rudolf Rigler, and Horst Vogel. The standard deviation in fluorescence correlation spectroscopy. *Biophysical Journal*, 80(6):2987–2999, 2001.

[103] Guanghua Wu, Haifeng Ji, Karolyn Hansen, Thomas Thundat, Ram Datar, Richard Cote, Michael F Hagan, Arup K Chakraborty, and Arunava Majumdar. Origin of nanomechanical cantilever motion generated from biomolecular interactions. *Proceedings of the National Academy of Sciences*, 98(4):1560–1564, 2001.

[104] Shiwei Wu, Gang Han, Delia J Milliron, Shaul Aloni, Virginia Altoe, Dmitri V Talapin, Bruce E Cohen, and P James Schuck. Non-blinking and photostable upconverted luminescence from single lanthanide-doped nanocrystals. *Proceedings of the National Academy of Sciences*, 106(27):10917–10921, 2009.

[105] Bo Zhang, Josiane Zerubia, and Jean-Christophe Olivo-Marin. Gaussian approximations of fluorescence microscope point-spread function models. *Applied Optics*, 46 (10):1819–1829, 2007.

TABLE I. Summary of notation.

Description	Variable	Units
Diffusion coefficient	D	μm^2/s
α parameter of the diffusion coefficient prior	α_D	-
β parameter of the diffusion coefficient prior	β_D	μm^2/s
Photon inter-arrival time	Δt	s
Total trace duration	T_{total}	s
Particle photon emission rate (maximum)	μ_{part}	photons/s
α parameter of the particle photon emission rate's prior	α_{part}	-
β parameter of the particle photon emission rate's prior	β_{part}	photons/s
Emission rate of biomolecule n at time t_k	μ_k^n	photons/s
Combined photon emission rate at time t_k	μ_k	photons/s
Background photon emission rate	μ_{back}	photons/s
Minor semi-axis of confocal PSF (focal plane)	ω_{xy}	μm
Major semi-axis of confocal PSF (optical axis)	ω_z	μm
Location of biomolecule n at time t_k in x-coordinate	x_k^n	μm
Location of biomolecule n at time t_k in y-coordinate	y_k^n	μm
Location of biomolecule n at time t_k in z-coordinate	z_k^n	μm
Recorded photon inter-arrival time between t_k and t_{k-1}	Δt_k	s
Load variable for biomolecule n	b^n	-
Prior weight for b_n	q^n	-
α parameter of prior weight q^n	α_q	-
β parameter of prior weight q^n	β_q	-
Upper bound for the number of model biomolecules	N	-
Mean value of initial biomolecule position's prior in the xy-plane	μ_{xy}	μm
Mean value of initial biomolecule position's prior on the z-axis	μ_z	μm
Variance of the initial biomolecule position's prior in the xy-plane	σ_{xy}^2	μm
Variance of the initial biomolecule position's prior on the z-axis	σ_z^2	μm
Normalized distance of biomolecule n at time t_k	d_k^n	-
Normalized distance for the ROI	ℓ	-
Volume of the ROI	V_ℓ	μm^3
Heaviside function	H	-
Periodic boundary in the xy-plane	L_{xy}	μm
Periodic boundary on the z-axis	L_z	μm

TABLE II. Probability distributions used and their densities. Here, the corresponding random variables are denoted by x.

Distribution	Notation	Probability density function	Mean	Variance
Normal	Normal(μ, σ^2)	$\frac{1}{\sqrt{2\pi\sigma^2}} e^{-\frac{(x-\mu)^2}{2\sigma^2}}$	μ	σ^2
Symmetric Normal	SymNormal(μ, σ^2)	$\frac{1}{2}\frac{e^{-\frac{(x+\mu)^2}{2\sigma^2}}}{\sqrt{2\pi\sigma^2}} + \frac{1}{2}\frac{e^{-\frac{(x-\mu)^2}{2\sigma^2}}}{\sqrt{2\pi\sigma^2}}$	0	$\mu^2 + \sigma^2$
Exponential	Exponential(λ)	$\lambda e^{-\lambda}$	λ	λ^2
Chi-square	$\chi^2(\alpha, 2)$	$\frac{1}{\Gamma(\frac{\alpha}{2})2^{\frac{\alpha}{2}}} x^{\frac{\alpha}{2}-1} e^{-\frac{x}{2}}$	α	2α
Gamma	Gamma(α, β)	$\frac{1}{\Gamma(\alpha)\beta^\alpha} x^{\alpha-1} e^{-\frac{x}{\beta}}$	$\alpha\beta$	$\alpha\beta^2$
Inverse-Gamma	InvGamma(α, β)	$\frac{\beta^\alpha}{\Gamma(\alpha)} x^{-\alpha-1} e^{-\frac{\beta}{x}}$	$\frac{\beta}{\alpha-1}$	$\frac{\beta^2}{(\alpha-1)^2(\alpha-2)}$
Beta	Beta(α, β)	$\frac{\Gamma(\alpha+\beta)}{\Gamma(\alpha)\Gamma(\beta)} x^{\alpha-1}(1-x)^{\beta-1}$	$\frac{\alpha}{\alpha+\beta}$	$\frac{\alpha\beta}{(\alpha+\beta)^2(\alpha+\beta+1)}$
Bernoulli	Bernoulli(q)	$(q-1)\delta_0(x) + q\delta_1(x)$	q	$q(1-q)$

TABLE III. Parameter values used in the generation of the synthetic traces. Choices are listed according to figures.

	L_{xy}	L_z	ω_{xy}	ω_z	N	D	μ_{part}	μ_{back}	T_{total}
Units	μm	μm	μm	μm	-	$\mu m^2/s$	photons/s	photons/s	s
Fig. (2(A))	1	2	0.3	1.5	1	1	4×10^4	10^3	0.03
Fig. (2(B))	1	2	0.3	1.5	2	1	4×10^4	10^3	0.03
Fig. (2(C))	1	2	0.3	1.5	3	1	4×10^4	10^3	0.03
Fig. (2(D))	1	2	0.3	1.5	4	1	4×10^4	10^3	0.03
Fig. (2(E))	1	2	0.3	1.5	5	1	4×10^4	10^3	0.03
Fig. (4(A))	1	2	0.3	1.5	4	1	4×10^4	10^3	0.03
Fig. (5(A))	1	2	0.3	1.5	10	1	4×10^4	10^3	0.03
Fig. (5(C))	1	2	0.3	1.5	4	1	4×10^4	10^3	0.03
Fig. (5(E))	1	2	0.3	1.5	1	1	4×10^4	10^3	0.03
Fig. (6)	1	2	0.3	1.5	4	10^{-2}	4×10^4	10^3	0.03
Fig. (6)	1	2	0.3	1.5	4	10^{-1}	4×10^4	10^3	0.03
Fig. (6)	1	2	0.3	1.5	4	1	4×10^4	10^3	0.03
Fig. (6)	1	2	0.3	1.5	4	10	4×10^4	10^3	0.03
Fig. (6)	1	2	0.3	1.5	4	100	4×10^4	10^3	0.03
Fig. (7(A))	1	2	0.3	1.5	4	1	4×10^5	10^3	0.03
Fig. (7(B))	1	2	0.3	1.5	4	1	4×10^4	10^3	0.03
Fig. (7(C))	1	2	0.3	1.5	4	1	4×10^3	10^3	0.03
Fig. (7(D))	1	2	0.3	1.5	4	1	10^3	10^3	0.03
Fig. (12(A))	1	2	0.3	1.5	10	10	4×10^5	10^3	0.05
Fig. (12(C))	1	2	0.3	1.5	10	10	4×10^4	10^3	0.05
Fig. (13(A))	1	2	0.3	1.5	10	10	4×10^5	10^3	0.05
Fig. (13(C))	1	2	0.3	1.5	10	10	4×10^4	10^3	0.05
Fig. (13(E))	1	2	0.3	1.5	10	10	4×10^3	10^3	0.05
Fig. (14)	1	2	0.3	1.5	10	10	4×10^4	10^3	0.05

TABLE IV. Parameter values used in the analyses of the traces. Choices are listed according to figures.

	ω_{xy}	ω_z	N	α_D	β_D	α_{part}	β_{part}	α_q	β_q	μ_{xy}	μ_z	σ^2_{xy}	σ^2_z
Units	μm	μm	-	-	$\mu m^2/s$	-	phts/s	-	-	-	μm	μm	μm^2
Fig. (2)	0.3	1.5	20	1	1	1	10^5	1	1	0.1	0.1	1	1
Fig. (4)	0.3	1.5	20	1	1	1	10^5	1	1	0.1	0.1	1	1
Fig. (5B)	0.3	1.5	20	1	1	1	10	1	1	0.1	0.1	1	1
Fig. (5D)	0.3	1.5	20	1	1	1	10	1	1	0.1	0.1	1	1
Fig. (5F)	0.3	1.5	20	1	1	1	10^5	1	1	0.1	0.1	1	1
Fig. (6)	0.3	1.5	20	1	1	1	10^5	1	1	0.1	0.1	1	1
Fig. (6)	0.3	1.5	20	1	1	1	10^5	1	1	0.1	0.1	1	1
Fig. (6)	0.3	1.5	20	1	1	1	10^5	1	1	0.1	0.1	1	1
Fig. (6)	0.3	1.5	20	1	100	1	10^5	1	1	0.1	0.1	1	1
Fig. (7A)	0.3	1.5	20	1	1	1	10^5	1	1	0.1	0.1	1	1
Fig. (7B)	0.3	1.5	20	1	1	1	10^5	1	1	0.1	0.1	1	1
Fig. (7C)	0.3	1.5	20	1	1	1	10^5	1	1	0.1	0.1	1	1
Fig. (7D)	0.3	1.5	20	1	1	1	10^5	1	1	0.1	0.1	1	1
Fig. (8)	0.3	1.5	20	1	1	1	10^5	1	1	0.1	0.1	1	1
Fig. (9)	0.3	1.5	20	1	1	1	10^5	1	1	0.1	0.1	1	1
Fig. (10)	0.3	1.5	20	1	1	1	10^5	1	1	0.1	0.1	1	1
Fig. (11)	0.221	3.90	20	1	100	1	10^5	1	1	0.1	0.1	1	1
Fig. (12)	0.3	1.5	20	1	1	1	10^5	1	1	0.1	0.1	1	1
Fig. (13)	0.3	1.5	20	1	1	1	10^5	1	1	0.1	0.1	1	1
Fig. (14)	0.3	1.5	20	1	1	1	10^5	1	1	0.1	0.1	1	1